Bioactive Materials 37 (2024) 378–392

Contents lists available at ScienceDirect

Bioactive Materials

journal homepage: www.keaipublishing.com/en/journals/bioactive-materials

MMP13-targeted siRNA-loaded micelles for diagnosis and treatment of posttraumatic osteoarthritis

Dongyang Zhou [a,b,d,e,1], Yan Wei [a,b,**,1], Shihao Sheng [c,1], Miaomiao Wang [a,b,i,1], Jiajing Lv [a,b,d], Bowen Zhao [a,b,d], Xiao Chen [c], Ke Xu [a,b], Long Bai [a,b], Yan Wu [a,b], Peiran Song [a,b], Liehu Cao [f], Fengjin Zhou [g,***], Hao Zhang [c,****], Zhongmin Shi [h,*****], Jiacan Su [a,b,c,*]

[a] Institute of Translational Medicine, Shanghai University, Shanghai, 200444, China
[b] National Center for Translational Medicine (Shanghai), Shanghai University, Shanghai, 200444, China
[c] Department of Orthopedic, Xin Hua Hospital, Shanghai Jiao Tong University School of Medicine, Shanghai, 200092, China
[d] College of Medicine, Shanghai University, Shanghai, 200444, China
[e] School of Environmental and Chemical Engineering, Shanghai University, Shanghai, 200444, China
[f] Department of Orthopedics, Shanghai Baoshan Luodian Hospital, Baoshan District, Shanghai, 201908, China
[g] Department of Orthopaedics, Honghui Hospital, Xi'an Jiao Tong University, Xi'an, 710000, China
[h] Department of Orthopedics, Sixth People's Hospital Affiliated to Shanghai Jiao Tong University, Shanghai, 200233, China
[i] Department of Rehabilitation Medicine, Shanghai Zhongye Hospital, Shanghai, 200941, China

ARTICLE INFO

Keywords:
Early-stage posttraumatic osteoarthritis (PTOA)
Matrix metalloprotease 13 (MMP 13)
Micelles
Fluorescence imaging
siRNA delivery

ABSTRACT

Posttraumatic osteoarthritis (PTOA) patients are often diagnosed by X-ray imaging at a middle-late stage when drug interventions are less effective. Early PTOA is characterized by overexpressed matrix metalloprotease 13 (MMP13). Herein, we constructed an integrated diagnosis and treatment micelle modified with MMP13 enzyme-detachable, cyanine 5 (Cy5)-containing PEG, black hole quencher-3 (BHQ3), and cRGD ligands and loaded with siRNA silencing MMP13 (siM13), namely ERMs@siM13. ERMs@siM13 could be cleaved by MMP13 in the diseased cartilage tissues to detach the PEG shell, causing cRGD exposure. Accordingly, the ligand exposure promoted micelle uptake by the diseased chondrocytes by binding to cell surface αvβ3 integrin, increasing intracellular siM13 delivery for on-demand MMP13 downregulation. Meanwhile, the Cy5 fluorescence was restored by detaching from the BHQ3-containing micelle, precisely reflecting the diseased cartilage state. In particular, the intensity of Cy5 fluorescence generated by ERMs@siM13 that hinged on the MMP13 levels could reflect the PTOA severity, enabling the physicians to adjust the therapeutic regimen. Finally, in the murine PTOA model, ERMs@siM13 could diagnose the early-stage PTOA, perform timely interventions, and monitor the OA progression level during treatment through a real-time detection of MMP13. Therefore, ERMs@siM13 represents an appealing approach for early-stage PTOA theranostics.

1. Introduction

Posttraumatic osteoarthritis (PTOA) is primarily induced by a mechanical joint injury [1]. The injuries frequently occur in military personnel and young athletes and lead to an accelerated pathology that necessitates surgical interventions 7–9 years earlier than primary OA [1–3]. Although PTOA only occupies ~12 % of OA cases in the world, it has led to a more severe socioeconomic burden due to affecting younger

Peer review under responsibility of KeAi Communications Co., Ltd.

* Corresponding author.
** Corresponding author.
*** Corresponding author.
**** Corresponding author.
***** Corresponding author.
E-mail addresses: ywei@shu.edu.cn (Y. Wei), dr.zhoufj@163.com (F. Zhou), zhcarl6@126.com (H. Zhang), 18930177323@163.com (Z. Shi), drsujiacan@163.com (J. Su).
[1] These authors contributed equally to this work.

https://doi.org/10.1016/j.bioactmat.2024.04.010
Received 28 February 2024; Received in revised form 9 April 2024; Accepted 10 April 2024

patients and its accelerated progression [4,5]. Currently, OA diagnosis primarily depends on patient-reported symptoms and X-ray imaging [6]. X-ray imaging is always considered the "gold standard," but it fails to detect early disease and subtle alterations [7]. The result led PTOA to be diagnosed in the middle-late stages when the therapeutic approaches are only limited to relieving symptoms, such as inflammation and pain [8]. Therefore, new strategies to diagnose and timely intervene in OA in its early stages are urgently needed.

The pathological change usually precedes the onset of clinical symptoms (i.e., joint pain and swelling on OA) [8,9]. Articular cartilage degeneration is one of the most significant characteristics of early-stage OA [10]. Articular cartilage comprises chondrocytes and extracellular matrix (ECM) [11]. Type 2 collagen (Col 2) is the primary structural protein of cartilage, establishing a network structure of ECM with aggrecan (ACAN) and other proteoglycans tangled within it [12]. Matrix metalloproteinase 13 (MMP13) is primarily responsible for degrading Col 2 [13], which is highly expressed in the articular cartilage of OA patients and almost undetectable in normal tissues [13]. In particular, in the murine PTOA model, MMP13 overexpression can initiate the onset of OA by excessively degrading Col 2 [14]. Moreover, MMP13 levels positively correlate with the presence of hypertrophic chondrocytes in early-stage OA [13,14]. Notably, in the murine PTOA model, MMP13 knockout mitigated the OA progression by protecting cartilage from Col 2 loss and structural disruption [15]. Therefore, MMP13 is a crucial biomarker for early-stage OA diagnosis and a central player in initiating the onset of OA and persistently promoting OA progression.

Fluorescence imaging can detect tumor-specific proteins and biological processes involved in oncogenesis through real-time imaging of tumor tissues [16]. Over the past decade, several tumor-specific fluorescent tracers have entered early-phase clinical trials [17]. Fluorescence imaging is adept at detecting abnormal biomarkers, showing a higher resolution for OA diagnosis than X-ray imaging [17]. Black hole quencher-3 (BHQ3) has maximal adsorption in the 620–730 nm range but has no native fluorescence. Accordingly, BHQ3 can quench fluorophores with emission wavelengths within this scope that are located at a distance of <10 nm [18], such as cyanine 5 (Cy5) and Cy 5.5 [19]. As an endopeptidase, MMP13 can cleave a specific peptide sequence (GPLG-VRG) [20]. Hence, we hypothesized that assembling BHQ3 and Cy5 *via* an MMP13-cleavable peptide spacer would achieve MMP13-triggered Cy5 fluorescence restoration with low background noise, enabling the facile visual detection of early-stage OA.

Besides precise diagnosis, timely intervention in upregulated MMP13 is crucial because persistent degradation of Col 2 pushes OA into the incurable middle-late stage [21]. The specific MMP13 inhibitor CL82198 has retarded OA progression and suppressed chondrocyte apoptosis by increasing Col 2 turnover [15]. Unfortunately, small-molecule inhibitors of MMPs in clinical trials induced musculoskeletal syndrome (MSS)-associated pain, leading to the trial discontinuation. The patients' MSS results from the inhibitor's nonspecific inhibition of multiple MMPs, such as MMP2, -3, -4, -7, and -9, which are crucial players in maintaining tissue homeostasis [22,23]. In contrast to small-molecule inhibitors, small interfering ribonucleic acids (siRNAs) can downregulate MMP13 more specifically because they silence target messenger RNAs (mRNAs) through base-pair complementation. However, free siRNAs face multiple delivery barriers after intraarticular injection. SiRNAs are easily cleared from the joints within several hours due to the small dimension (approximately 13–14 KDa) and undergo nuclease degradation in extracellular space [11,24]. Moreover, these highly negatively charged macromolecules cannot pass through negatively charged cellular membranes [25,26]. Therefore, delivering intact siRNAs to diseased chondrocytes at sufficient levels remains a significant challenge. Encapsulation with nanovehicles has been revealed to prolong the articular retention of payloads [11]. Healthy and diseased chondrocytes universally express αvβ3 integrins [27,28], which can mediate the cell internalization of Arg-Gly-Asp (RGD)-modified nanovehicles *via* ligand-receptor interaction [29–31]. Modification with the flexible and hydrophilic long PEG chains can shield the ligands on the nanovehicle surface, protecting the nanovehicles from nonspecific uptake [32,33]. Therefore, we supposed that a nanovehicle modified with RGD ligands shielded by an MMP13-detachable PEG shell would achieve selective and on-demand internalization by diseased chondrocytes *via* MMP13-mediated deprotection. Moreover, if Cy5 and BHQ3 were fixed in the detachable PEG motif and the main body of nanovehicles, respectively, the MMP13-triggered PEG detachment would induce Cy5 fluorescence restoration for real-time detecting diseased chondrocytes.

With the above-mentioned considerations in mind, we synthesized MMP13 enzyme-detachable PEG (EP), its lipid conjugate DSPE-PEG_{2000}-EP, DSPE-PEG_{2000}-BHQ3, and DSPE-PEG_{2000}-cRGDfK. With these major lipid components and the cationic lipid *N*-[1-(2,3-dioleoyloxy)propyl]-N,N,N-trimethylammonium methylsulfate (DOTAP), we prepared MMP13 enzyme-activated, cRGDfK-modified micelles loaded with siRNAs silencing MMP13 (siM13), i.e., ERMs@siM13 (Scheme 1). Upon activation by MMP13 overexpressed by diseased chondrocytes in early-stage PTOA, ERMs could detach Cy5-containing PEG shells. By separating from BHQ3, Cy5 restored its fluorescence for early-stage OA diagnosis. The exposed cRGD promoted the micelle uptake by diseased chondrocytes to downregulate MMP13 accordingly, thus retarding PTOA progression. Moreover, as the treatment was pursued, the micelles could monitor the therapeutic efficacy in real-time, substantially facilitating physicians to adjust the treatment regimen in time in clinical practice.

2. Materials and methods

2.1. Materials

1,2-distearoyl-sn-glycero-3-phosphoethanolamine-*N*-[methoxy (polyethylene glycol) −2000] (DSPE-PEG_{2000}) and DSPE-PEG_{2000}-NH_2 were purchased from Bide Pharmaceutical Technology Co., Ltd. (Shanghai, China). Cyanine 5 (Cy5)-C(PEG_{2000})-GPLGVRGK-NH_2 (i.e., EP) and Cy5-C(PEG_{2000})-GplgvrGK-NH_2 (i.e., nEP) were synthesized by Anhui Guoping Pharmaceutical Co. Ltd. (Anhui, China), the successful synthesis of which was confirmed *via* matrix-assisted laser desorption ionization time-of-flight (MALDI-TOF)/mass spectrum (MS). Various siRNAs silencing MMP13 (siM13s) were synthesized by BioTNT Co. Ltd. (Shanghai, China): siRNA-1: 5′-GGAGUUAUGAUGAUGUUAATT-3'; siRNA-2: 5′- GAGAAACUAUGAUCUUUAATT-3'; siRNA-3: 5′-CAAAGUAGAUGCUGUCUAUTT-3'. Lipofectamine 3000 and LysoTracker Red were purchased from Invitrogen (NY, USA). Recombinant human MMP13 proenzyme (511-MM-010) was ordered from the R&D Systems Co., Ltd. (Minnesota, USA). DSPE-PEG_{2000}-NHS was bought from Peng Sheng Biological Co., Ltd. (Shanghai, China). DSPE-PEG_{2000}-c (RGDfK) (DSPE-PEG-cRGD) was obtained from Ruixibiotech Co., Ltd. (Xi'an, China). BHQ3-NHS was bought from Changsha Hanchen Biotechnology Co., Ltd. (Changsha, China). DOTAP was obtained from AVT Pharmaceutical Tech Co., Ltd. (Shanghai, China). Deuterium oxide (D_2O) was bought from Adamas-beta Co., Ltd. (Shanghai, China). Cell Counting Kit-8 (CCK-8) and the BeyoClick™ EdU Cell Proliferation Kit with Alexa Fluor 647 were obtained from Beyotime Biotechnology Co. Ltd. (Shanghai, China). Coumarin 6 (C6) and 1,1-dioctadecyl-3,3,3,3-tetramethylindotricarbocyaineiodide (DiR) were obtained from Yeasen Biotechnology Co., Ltd. (Shanghai, China). The dialysis bag (MWCO: 3500 Da) was purchased from Viskase Co., Ltd. (USA). A mouse MMP13 Enzyme-linked immunosorbent assay (ELISA) kit was acquired from Biolegend Co., Ltd. (California, USA). Unless otherwise specified, all other reagents were obtained from Macklin Reagent Co., Ltd. (Shanghai, China).

2.2. Formulation optimization and characterization of ERMs@siM13

2.2.1. Preparation of ERMs@siM13

ERMs@siM13 was prepared using a thin-film hydration method, as

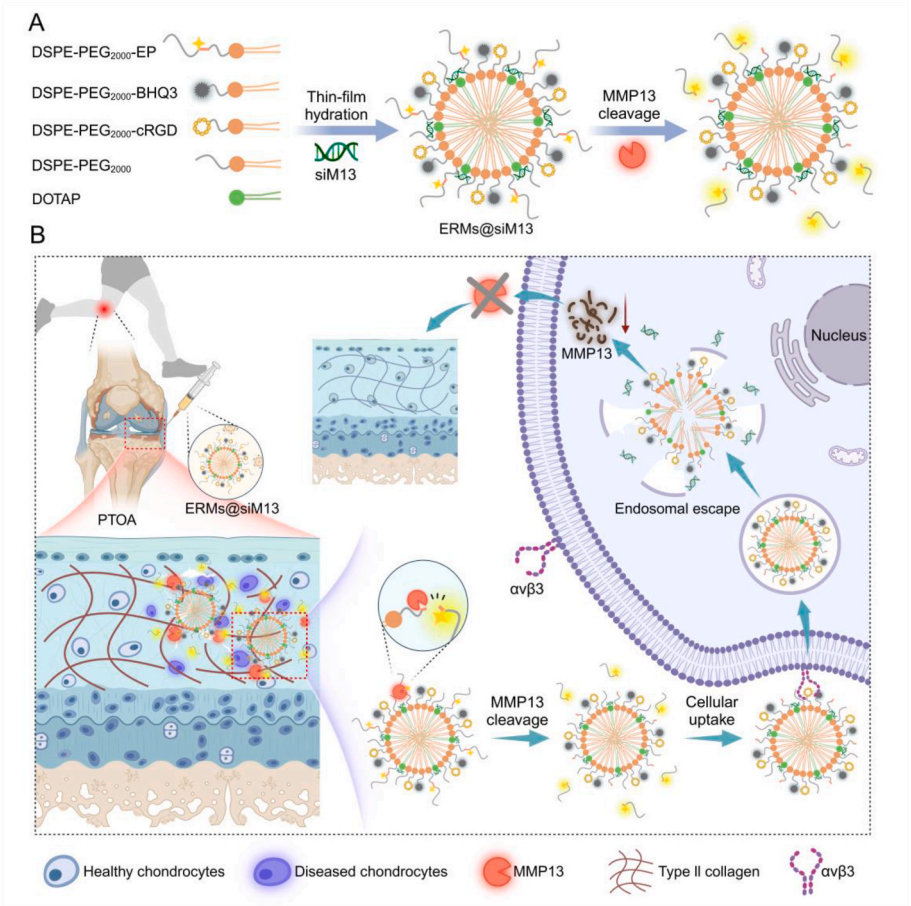

Scheme 1. Proposed action mechanism of ERMs@siM13 in the early-stage posttraumatic osteoarthritis (PTOA) mouse model. (A) Schematic illustration of preparation procedure of ERMs@siM13 and its matrix metalloproteinase 13 (MMP13)-mediated activation. (B) After intraarticular injection into the joints with early-stage PTOA, ERMs@siM13 can be activated by MMP13 overexpressed surrounding diseased chondrocytes, detaching the Cy5-bearing PEG protective shell. Accordingly, cRGD is exposed to promote the siRNA silencing MMP13 (siM13)-loaded micelle uptake by the diseased cells for on-demand MMP13 downregulation, and Cy5 fluorescence is restored to report the diseased state of cartilage tissues.

previously reported [34,35]. Briefly, the lipid components of DSPE--PEG_{2000}-cRGD, DSPE-PEG_{2000}-EP, DSPE-PEG_{2000}-BHQ3, DSPE-PEG_{2000}, and DOTAP (DSPE-PEG_{2000}-cRGD: DSPE-PEG_{2000}-EP: DSPE--PEG_{2000}-BHQ3: DSPE-PEG_{2000}: DOTAP = X_1:X_2:X_3:100-X_1-X_2-X_3:8, mol: mol) were dissolved in chloroform. The organic solvents were removed through rotary evaporation under vacuum, forming a lipid thin film. Then, FAM-siRNA/siM13 dissolved in phosphate buffer solution (PBS, pH 7.4) was added to hydrate the thin lipid film and form micelles. The micelles were purified with preparative HPLC through a size-exclusion chromatography (SEC) column (YMC-Pack Diol-120/S, Japan) using a mobile phase of PBS (pH = 7.0–7.2) to remove free EPs and unloaded siM13s. nERMs@siM13 were prepared using the same procedure except for replacing DSPE-PEG_{2000}-EP with DSPE-PEG_{2000}-nEP.

2.2.2. Optimizing modification density of DSPE-PEG_{2000}-cRGD

C6-labeled cRGD-modified micelles (i.e., RMs@C6) micelles with varied cRGD density were prepared with DSPE-PEG_{2000}-cRGD, DSPE-PEG_{2000}, DOTAP, and C6 (DSPE-PEG_{2000}-cRGD: DSPE-PEG_{2000}: DOTAP: C6 = x:100-x:8:0.5, mol: mol; x = 5, 10, and 15) following the above-mentioned procedure. Then, the modification density of DSPE-PEG_{2000}-cRGD was optimized *via* cell uptake.

Primary chondrocytes were extracted from the C57 mice (1-5-day-old), as previously reported, with minor modifications [36]. Briefly, the femoral condyles and tibial plateaus were soaked in PBS containing streptomycin (100 μg/mL) and penicillin (100 U/mL) for 5 min, cut into pieces, and digested for 12 h in 2 mg/mL of type II collagenase. The chondrocytes were collected and maintained in the DMEM/F-12 complete medium. The attached cells were considered primary chondrocytes, and passages 0 to 3 of these cells were used for subsequent assay.

The primary chondrocytes were seeded in 24-well plates at a density of 1.0×10^5 cells/well for adherence, and fresh medium containing IL-1β (10 ng/mL) was added to induce the cells for 48 h. Then, the diseased cells were treated with RMs@C6 with various cRGD modification densities at a C6 final concentration of 0.5 μg/mL for 2 h. The chondrocytes were collected and resuspended in PBS for flow cytometry analysis (CytoFlex3, Beckman Coulter, USA). The DSPE-PEG_{2000}-cRGD modification density of x = 10 was selected to maximize chondrocyte uptake.

2.2.3. Optimizing modification density of DSPE-PEG_{2000}-nEP

The cRGD shielding effects by nEP were optimized *via* cellular uptake. The nERMs@C6 micelles were prepared with the lipid components of DSPE-PEG_{2000}-cRGD, DSPE-PEG_{2000}-nEP, DSPE-PEG_{2000}, DOTAP, and C6 (DSPE-PEG2000-cRGD: DSPE-PEG_{2000}-nEP: DSPE-PEG_{2000}: DOTAP: C6 = 10:x:90-x:8:0.5, mol: mol, x = 0, 2.5, 5, 10, and 20).

Primary chondrocytes were extracted and induced with IL-1β for 48 h, as mentioned above. Various nERMs@C6 formulations containing different modification densities of DSPE-PEG_{2000}-nEP were added to the cells for 2 h of incubation. Then, the chondrocytes were collected for flow cytometry analysis (CytoFlex3, Beckman Coulter, USA). The DSPE-PEG_{2000}-nEP modification density of x = 10 was selected to maximize cRGD shielding.

2.2.4. Optimizing modification density of DSPE-PEG$_{2000}$-BHQ3

The modification density of DSPE-PEG$_{2000}$-BHQ3 was optimized by maximizing its fluorescence quenching effects on Cy5-containing EPs. ERMs were prepared with the lipid components of DSPE-PEG$_{2000}$-cRGD, DSPE-PEG$_{2000}$-EP, DSPE-PEG$_{2000}$-BHQ3, DSPE-PEG$_{2000}$, and DOTAP (DSPE-PEG$_{2000}$-cRGD: DSPE-PEG$_{2000}$-EP: DSPE-PEG$_{2000}$-BHQ3: DSPE-PEG$_{2000}$: DOTAP = 10:10:x:80-x:8, mol: mol, x = 0, 5, 10, and 20), as described above. Accordingly, the DSPE-PEG$_{2000}$-EP-free formulation served as a control. The fluorescence signal of Cy5 was captured through *in vivo* spectrum imaging system (λex/em = 605/680 nm) (AniView100, BLT, China) and a microplate reader (λex/em = 605/650–800 nm) (Infinite®200 PRO, Tecan, Switzerland). The DSPE-PEG$_{2000}$-BHQ3 modification density of x = 20 was selected to maximize Cy5 fluorescence quenching.

2.2.5. Screening of siM13 sequences

Three siM13 sequences were synthesized to transfect diseased chondrocytes and *mmp13* RNA expression was measured *via* RT-qPCR assay. Briefly, diseased chondrocytes were induced, as mentioned above. The siRNAs were mixed with Lipofectamine 3000 in DMEM/F12 complete medium and added to diseased chondrocytes for 24 h of incubation at a final siM13 concentration of 5 μg/mL. Subsequently, the total RNA was extracted using Trizon reagent (Cwbio, China), and the cDNA was obtained through a reverse transcription kit (Takara#RR036A, Takara Bio USA). The RT-qPCR assay was performed using TB Green Premix Ex Taq II (Tli RNaseH Plus) (RR820, Takara Bio, USA) at the qTOWER^3 real-time PCR system (Analytik Jena, Jena, Germany). GAPDH served as an internal reference. The relative expression of *mmp13* mRNA was calculated using the $2^{-\Delta\Delta Ct}$ methodology.

2.2.6. Characterization of ERMs@siM13

The morphology of ERMs@siM13 was observed under a transmission electron microscope (TEM) (JEM-1400 Flash, Japan). ERMs@siM13 and nERMs@siM13 were incubated with MMP13 for 1 h at 37 °C according to 136 μg peptide corresponding to 0.08 μg MMP13. The ERMs@siM13 and nERMs@siM13 before and after enzymatic cleavage were analyzed by an *in vivo* spectrum imaging system to evaluate the MMP13 tracking ability of ERMs@siM13. The FAM-siRNA content in ERMs, nERMs, and RMs at various N/P ratios was measured through a microplate reader (Cytation 5, BioTek, USA) after the micelle structure was disrupted with 2 % Triton X-100. The encapsulation efficiency (EE) of siRNA was calculated with the following equation (1).

$$\text{EE}\ (\%) = \frac{\text{amount of siRNA loaded in the micelles}}{\text{amount of the feeding siRNA}} \times 100\% \quad (1)$$

To study the protective effects of ERMs@siM13 on siMP 13 from nuclease degradation, nERMs@siMMP13, ERMs@siM13, RMs@siM13, and free siM13 were incubated with 50 % fetal bovine serum (FBS) at 37 °C. After preset intervals, the samples were collected and cooled at −80 °C. Then, the micelles were disrupted with 2 % Triton X-100, followed by the electrophoresis assay using a 2 % agarose gel at an equivalent siM13 amount of 0.1 μg/well. The electrophoresis was performed at 120 kV for 20 min. The agarose gel was imaged by UV illumination and photographed under a ChemiDoc MP imaging system (Bio-Rad, USA).

2.3. Cell delivery of ERMs@siM13

2.3.1. Diagnostic capability of ERMs for diseased chondrocytes

Diseased chondrocytes were induced by IL-1β for 48 h, as described above. ERMs and nERMs were added to the diseased chondrocytes at a Cy5 final concentration of 1.0 μg/mL for 2 h of incubation. Normal chondrocytes serve as a control. The cells in the plates were directly imaged with an *in vivo* spectrum imaging system (AniView100, BLT, China).

2.3.2. Cellular uptake assay of ERMs@C6

To evaluate the MMP13-activated uptake behavior of ERMs@C6, Ms@C6, RMs@C6, nERMs@C6, and ERMs@C6 were added to the diseased chondrocytes at a C6 final concentration of 0.5 μg/mL for 2 h of incubation in the dark. Then, the cells were collected for flow cytometry assay.

Confocal imaging was also performed to visually observe the cellular uptake of ERMs@C6. Briefly, the diseased chondrocytes were treated with various C6-labeled formulations, as described above. Then, the cells were washed with PBS and fixed in 4 % paraformaldehyde (PFA) for 15 min. The nuclei were counterstained with 4′, 6-diamidino-2-phenylindole (DAPI) for 5 min. The cells were imaged by confocal laser scanning microscopy (CLSM) (FV3000, Olympus, Japan).

2.3.3. Endosomal escape assay

FAM-siRNA-loaded ERMs were incubated with diseased chondrocytes for 1 h at a final FAM-siRNA concentration of 100 nM. Then, the medium was replaced with a fresh culture medium, and incubation continued for 1, 4, and 8 h. At 30 min before each time point, LysoTracker Red was added to label late endosomes/lysosomes. Subsequently, the cells were fixed in 4 % PFA for 15 min, and the nuclei were stained with DAPI. Then, the cells were observed by CLSM (FV3000, Olympus, Japan). The colocalization coefficients of endosomes/lysosomes and FAM-siRNAs were calculated using ImageJ software.

2.4. Diagnostic and treatment effects of ERMs@siM13 on diseased chondrocytes

2.4.1. Diagnostic ability of ERMs@siM13 for in vitro treatment efficacy

The diseased chondrocytes were induced by IL-1β for 48 h and treated with nERMs@siM13, ERMs@siM13, and free siM13 for 24 h at an siM13 final concentration of 5 μg/mL. Then, ERMs were added to the treated cells for 2 h of incubation and imaged using an *in vivo* spectrum imaging system.

2.4.2. RT-qPCR assay

The diseased chondrocytes were treated with free siM13, ERMs@siM13, and nERMs@siM13 (siM13: 5 μg/mL), as described above. Then, *mmp13* mRNA expression was detected *via* q-PCR assay.

2.4.3. Western blot analysis

The diseased chondrocytes were treated as described above. Normal chondrocytes served as a control. Then, the cells were lysed using RIPA Lysis Buffer (Beyotime, China). The lysis solution was centrifuged at 12,000×*g* for 15 min at 4 °C to harvest the supernatants. The protein levels in the supernatants were measured using a BCA protein assay kit. The samples were loaded onto a 10 % SDS-PAGE gel at an equivalent protein amount (40 μg) and separated *via* electrophoresis. Then, the proteins were transferred onto polyvinylidene fluoride (PVDF) membranes. The membranes were blocked by 5 % non-fat milk in TBS containing 0.1 % Tween-20 (TBST) for 2 h and then probed with the primary antibodies against MMP13 (1:500, GB11247-1, Servicebio, China) and Col 2 (1:1000, GB11021, Servicebio, China) overnight at 4 °C. GAPDH served as an internal reference. After washed thrice with TBST, the membranes were then incubated with goat anti-rabbit IgG-HRP (1:5000, GB23303, Servicebio, China)) and visualized using a ChemiDoc MP imaging system (Bio-Rad, USA).

2.4.4. Immunofluorescence imaging assay

The diseased chondrocytes were treated, as mentioned above. Healthy chondrocytes served as a normal control. The chondrocytes were fixed in 4 % PFA and incubated with the primary antibodies against MMP-13 (1:250, 18165-1-AP, Proteintech, USA) and Col 2 (1:250, 28459-1-AP, Proteintech, USA) overnight at 4 °C. Next, the cells were incubated in the dark with Alexa Fluor 488-conjugated goat anti-rabbit IgG (1:1000, ab150077, Abacm, USA) for 1 h. The nuclei were stained

with DAPI. The MMP13 expression was imaged under a fluorescence microscope (ECLIPSE Ci-L, Nikon, Japan), and the Col 2 expression was observed by CLSM (FV3000, Olympus, Japan). The fluorescence intensity was quantified using ImageJ software.

2.4.5. Cell proliferation assay

The diseased chondrocytes were induced and treated, as mentioned above. Then, the chondrocyte proliferation was evaluated *via* EdU staining (BeyoClick™ EdU-647, Beyotime, China) following the manufacturer's protocols.

2.5. Animals

Male C57 mice (6–7 weeks old) were purchased from Changzhou Cavens Experimental Animal Co., Ltd. (Jiangsu, China). The mice were kept at 20–25 °C and 50 % humidity with a 12 h light/dark cycle. They were provided with unrestricted access to water and rodent chow. All animal experiments were performed following the protocols approved by the ethics committee of Shanghai University (NO. ECSHU 2023–101).

2.6. In vivo retention assay of ERMs@DiR

C57 male mice were subjected to destabilized medial meniscus (DMM) surgery on the right knees and sham surgery on the left knees to establish PTOA models. Briefly, the joint capsules of mice were swiftly opened following anesthesia, and the medial meniscotibial ligament was incised to destabilize the meniscus without damaging the surrounding tissues. Two weeks later, ERMs@DiR and nERMs@DiR were intraarticularly administered at a DiR dose of 0.2 μg/mouse. Then, the mice were imaged using an *in vivo* spectrum imaging system (AniView100, BLT, China) at the predetermined time points (DiR: λex/em = 780/820 nm).

2.7. Monitoring PTOA progression by ERMs during treatment

To monitor PTOA progression during treatment, a murine PTOA model was established through DMM surgery, as described above. At 2 weeks post-surgery, the PTOA mice were intraarticularly administered with nERMs@siM13 and ERMs@siM13 at a siM13 dose of 10 μg/mouse. The treatment was then repeated every 5 days for 9 cycles. The ERMs were injected into the articular cavity for diagnosis at 17, 32, 42, and 57 d post-surgery, and the Cy5 fluorescence signal was captured with an *in vivo* spectrum imaging system.

2.8. MMP13 expression in PTOA mice during treatment

Immunofluorescence staining of MMP13 was performed during treatment to confirm the diagnosis mechanism of ERMs. Briefly, the PTOA mice were treated with siM13-containing formulations, as mentioned above. At 17, 32, 42, and 57 d post-surgery, the mice were sacrificed to collect the joints for fixation in 4 % PFA and subsequent paraffin sectioning. Paraffin sections (6-μm thickness) were subjected to immunofluorescence staining of MMP13, as described above. Fluorescence images were captured by CLSM (FV3000, Olympus, Japan) and quantified with ImageJ software.

2.9. Therapeutic efficacy of ERMs@siM13 in the murine PTOA model

2.9.1. ERMs@siM13 administration

The murine PTOA model was generated, as mentioned above. The mice were randomly divided into 5 groups and intraarticularly injected with PBS, free siM13, RMs@siM13, nERMs@siM13, and ERMs@siM13 at a siM13 dose of 10 μg/mouse (dissolved or suspended in PBS). Treatment was performed every 5 days for 4 or 8 weeks. At the end of treatment, the animals were sacrificed to remove the joints, which were fixed in 4 % PFA for subsequent analysis.

2.9.2. Histological evaluation of cartilages

The fixed joints were decalcified in 0.5 M EDTA (pH = 7.4) (G1105, Servicebio, China) for 2 weeks. The samples were then embedded in paraffin and sectioned into 6-μm slices along the sagittal plane. The slices were stained with hematoxylin-eosin (H&E) (Solarbio, China) and safranin O/fast green (Solarbio, China). The stained slices were then imaged on a fluorescence microscope (ECLIPSE Ci-L, Nikon, Japan) to visualize the cartilage tissue morphology. The Mankin score was adopted to evaluate the treated tissues [37,38].

2.9.3. Micro-computed tomography (Micro-CT)

The fixed joints were scanned with a SkyScan 1275 CT scanner (Bruker, Germany), and the application software (DataViewer and CTAn) was used to evaluate and analyze relevant parameters.

2.9.4. Immunohistochemical (IHC) analysis

Paraffin sections of the articular tissues were subjected to IHC analysis. Briefly, after antigen retrieval, the samples were incubated with primary antibodies, including rabbit *anti*-MMP13 (1:250, GB11247, Servicebio, China), Col 2 (1:250, GB11021, Servicebio, China), and ACAN (1:500, GB11373, Servicebio, China) overnight at 4 °C, followed by binding with biotinylated secondary antibodies and incubation with diaminobenzidine (DAB) substrate for 10 min. The samples were imaged under the fluorescence microscope (ECLIPSE Ci-L, Nikon, Japan). The positive areas of MMP13, Col 2, and ACAN were quantified through ImageJ software.

2.10. Biosafety analysis

The healthy C57 mice were intraarticularly injected with a single dose of PBS, ERMs@siM13, nERMs@siM13, RMs@siM13, and free siM13. On the fifth day postinjection, the joints were collected and processed for H&E staining to evaluate local synovium irritation.

The PTOA mice were treated every 5 days for 12 cycles, as described above. Then, the major organs (kidney, liver, lung, heart, and spleen) and the blood samples were collected. The blood samples were subjected to a routine blood examination and blood biochemical assay. The major organs were processed for H&E staining.

2.11. Statistical analysis

All the data were presented as the mean ± SD. Significant differences were assessed with Student's unpaired *t*-test, and three or more independent groups were compared by nonparametric two-tailed analysis of variance, followed by Tukey's post hoc test. Under all conditions, a *p*-value $\leq$0.05 is considered statistical significance. The analysis was performed with GraphPad Prism 8.4.3 software.

3. Results

3.1. Synthesis of DSPE-PEG$_{2000}$-EP and DSPE-PEG$_{2000}$-BHQ3

To obtain an MMP13-detachable PEG shell, we synthesized EPs (Cy5-C(PEG$_{2000}$) GPLGVRGK) that contained MMP13-sensitive peptide motif (GPLG-VRG) [20], fluorescent dye Cy5, and PEG$_{2000}$. First, the successful synthesis of Cy5-CGPLGVRGK was confirmed by detecting two multiply charged ion peaks in the MS spectrum, and its purity was above 95 % based on the HPLC/UV analysis (Fig. S1A). Similarly, Cy5-CGplgvrGK, a MMP13-insensitive counterpart, was also successfully synthesized (Fig. S1B). Moreover, the H NMR spectra showed that the characteristic peaks of PEG$_{2000}$-mal (a) and Cy5-CGPLGVRGK/Cy5-CGplgvrGK (b, b', c, and c') simultaneously appeared in the spectrum of EP/nEP, confirming their successful synthesis (Fig. S2).

EPs are expected to be cleaved by MMP13 overexpressed in OA cartilage tissues at the position of G-V within the peptide sequence [13,

20]. After 2 h of incubation with MMP13, no degradation peak appeared in the HPLC spectrum of nEP (Fig. 1A). In contrast, EP generated a new peak at a retention time (t_R) of 18.75 min, suggesting its MMP13 responsiveness.

Then, the obtained EP/nEP was conjugated with DSPE-PEG$_{2000}$-NHS *via* acylation reactions to yield DSPE-PEG$_{2000}$-EP/nEP. The conjugating efficiency of EP (nEP) was 33.24 % (35.63 %), determined through HPLC/UV.

DSPE-PEG$_{2000}$-BHQ3 was synthesized by conjugating BHQ3-NHS to DSPE-PEG$_{2000}$-NH2 *via* acylation reactions. DSPE-PEG$_{2000}$-BHQ3 had a UV spectrum comparable to BHQ3 (Fig. S3). Moreover, the H NMR spectra revealed that the characteristic peaks of BHQ3-NHS (9.70 ppm (a), 9.49 ppm (b), and 6.98 ppm (c)) and DSPE-PEG$_{2000}$-NH2 (3.58 ppm (d)) simultaneously appeared in the spectrum of DSPE-PEG$_{2000}$-BHQ3 (Fig. S4). Collectively, these results confirmed the successful synthesis of DSPE-PEG$_{2000}$-BHQ3.

3.2. Formulation optimization of ERMs@siM13

The diagnosis- and treatment-integrated micelle ERMs@siM13 was designed based on the following considerations. In the MMP13-deficient region, EPs are expected to shield cRGD ligands through the PEG layer, protecting the micelles from nonspecific uptake by healthy chondrocytes that also express αvβ3 integrin at a certain level [27,28,39–41]. Meanwhile, the fluorescence signal of Cy5 in EPs is quenched by BHQ3 [19]. Upon reaching the diseased chondrocytes overexpressing MMP13, the Cy5-containing PEG motif is detached by MMP13 cleavage to restore the fluorescence signal due to the separation from BHQ3 on the micelles.

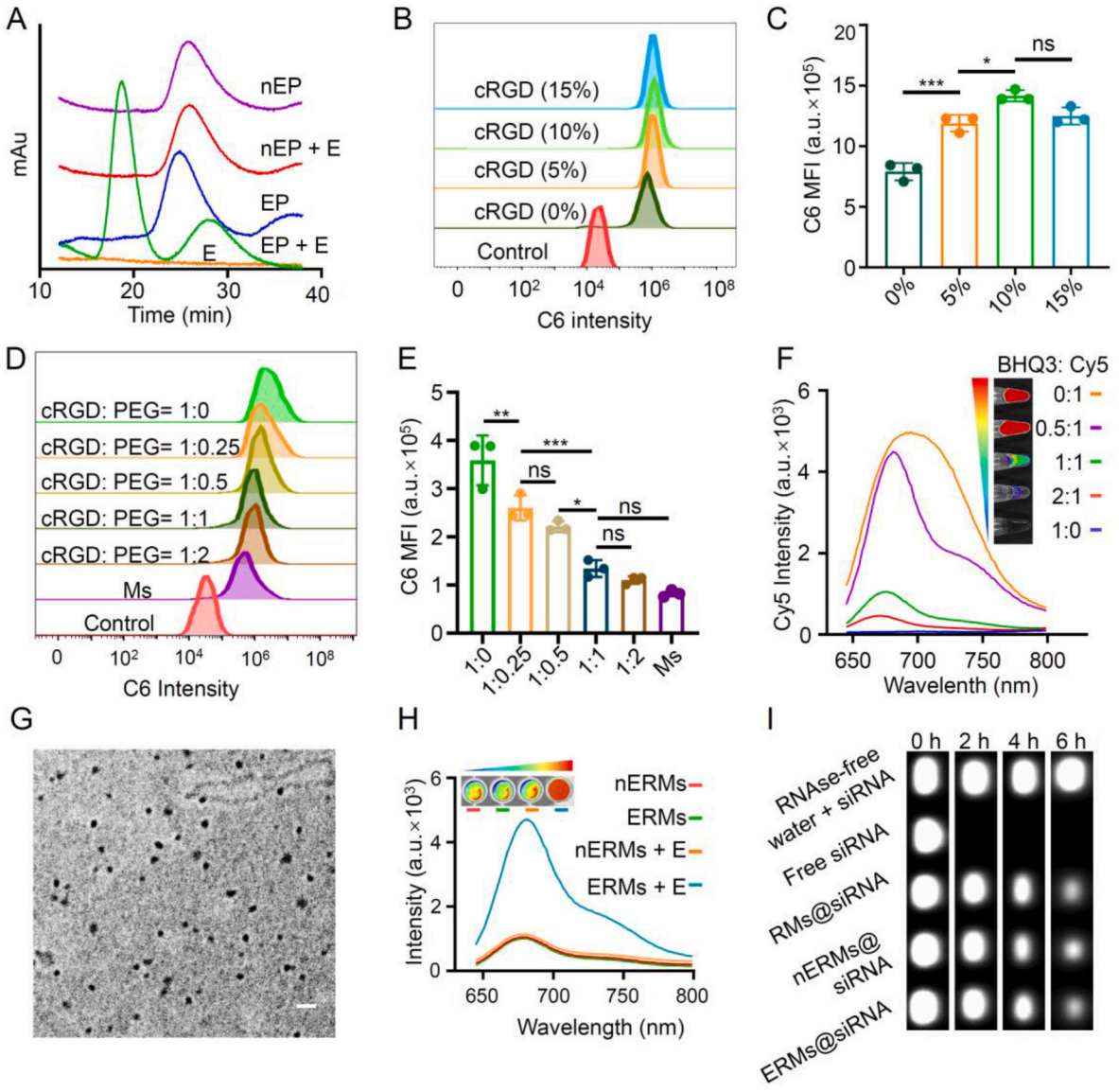

Fig. 1. Preparation and characterization of ERMs@siM13. (A) High-performance liquid chromatography (HPLC) spectra of Cy5-C(PEG$_{2000}$)-GPLGVRGK-NH$_2$ (EP) and Cy5-C(PEG$_{2000}$)-GplgvrGK-NH$_2$ (nEP) before and after incubation with matrix metalloproteinase 13 (MMP13). (B) Representative flow cytometry histogram showing the uptake of coumarin 6 (C6)-labeled RMs with various cRGD modification densities by diseased chondrocytes and (C) the corresponding mean fluorescence intensity (MFI) of C6. (D) Representative flow cytometry histogram showing the internalization of nERMs@C6 with various ratios of cRGD: PEG by diseased chondrocytes and (E) the corresponding C6 MFI. (F) Representative fluorescence spectra and fluorescence images of nERMs containing various molar ratios of BHQ3-to-Cy5. (G) Representative transmission electron microscopy (TEM) images of ERMs@siM13. Scale bar: 50 nm. (H) Representative fluorescence spectra and fluorescence images of ERMs and nERMs before and after incubation with MMP13. (I) Serum stability of siM13 loaded by RMs, ERMs, and nERMs determined through agarose gel electrophoresis. Free siM13 served as the controls. "E" represents MMP13. Data are presented as mean ± SD. $^*P < 0.05$, $^{**}P < 0.01$, $^{***}P < 0.001$, and ns, no significant difference among the marked groups using nonparametric two-tailed analysis of variance.

Meanwhile, the cRGD exposure promotes the micelle uptake by hypertrophic chondrocytes. To achieve these desirable functions, we performed extensive formulation optimization by screening the feeding ratios of DSPE-PEG_{2000}-cRGD, DSPE-PEG_{2000}-nEP, and DSPE-PEG_{2000}-BHQ3.

ERMs@siM13 was prepared through thin-film hydration and purified by preparative HPLC (Scheme. 1A). Modification density of cRGD in RMs was optimized by changing the feeding ratios of DSPE-PEG_{2000}-cRGD (i.e., 0, 5, 10, and 15 mol%) to maximize the micelle uptake by diseased chondrocytes. The flow cytometry assay revealed that cellular internalization of RMs@C6 gradually increased as cRGD modification density was elevated from 0 to 10 mol% (Fig. 1B and C). However, cellular internalization of RMs@C6 was not significantly different between 10 mol% and 15 mol% of cRGD. Therefore, the DSPE-PEG_{2000}-cRGD feeding ratio of 10 mol% was selected for subsequent assay.

Subsequently, the DSPE-PEG_{2000}-nEP ratio in nERMs was further optimized for more effective cRGD shielding. nERM internalization by diseased chondrocytes continuously declined with the improvement in the nEP feeding ratios due to elevated cRGD shielding (Fig. 1D and E). However, when the molar ratio of DSPE-PEG_{2000}-nEP-to-DSPE-PEG_{2000}-cRGD increased from 1:1 to 1:2, the uptake efficiency of nERMs was not significantly different, which was even comparable to that of bare micelle Ms. These results suggest that 10 mol% of DSPE-PEG_{2000}-nEP could shield the cRGD ligands on the nERMs completely, which was selected for the follow-up assay.

BHQ3 is a non-fluorescent dark quencher with maximal fluorescent absorption ranging from 620 to 730 nm [42]. Hence, it effectively quenches the fluorescence of fluorophores emitting within this spectrum, such as Cy5 (λex/em = 635/675 nm). The DSPE-PEG_{2000}-BHQ3 feeding ratio in nERMs was further optimized to maximize the Cy5 fluorescence quenching. When the BHQ3-to-Cy5 molar ratio increased to 2:1, Cy5 fluorescence intensity substantially decreased (Fig. 1F). Moreover, the Cy5 fluorescence signal at this ratio was almost invisible in the fluorescence images. Hence, the DSPE-PEG_{2000}-BHQ3 feeding ratio of 20 mol% was selected.

siM13 sequences were screened through RT-qPCR assay (Fig. S5). Compared to PBS control (100 %), siM13-1 reduced *mmp13* mRNA expression to 30.7 %, far lower than siM13-2 (70.0 %) and siM13-3 (47.3 %). Therefore, the siM13-1 sequence 5′-GGAGUUAUGAUGAUGUUAATT-3′ was selected.

When the feeding amount of siM13 was increased from 10:1 to 8:1 (N/P ratio), EE of siM13 by ERMs, nERMs, and RMs was still maintained at approximately 90 %. However, as the siM13 feeding amount was further improved to 6:1 (N/P ratio), its EE substantially decreased to approximately 55 % (Table S1). Hence, a feeding ratio of 8:1 (N/P ratio) was selected.

3.3. Characterization of the optimized ERMs@siM13 formulation

The optimized final formulation of ERMs@siM13 contained DSPE-PEG_{2000}-cRGD, DSPE-PEG_{2000}-EP, DSPE-PEG_{2000}-BHQ3, DSPE-PEG_{2000}, and DOTAP at a molar ratio of 10:10:20:60:8. The ERMs@siM13 micelles exhibited a uniform particle size of approximately 20 nm with a spherical morphology (Fig. 1G). The zeta potentials of ERMs@siM13, nERMs@siM13, and RMs@siM13 were 0.15 ± 1.04, 0.18 ± 1.07, and −0.41 ± 0.64 mV, respectively. The neutral surfaces would facilitate the micelles to penetrate the negatively charged cartilage matrix.

The MMP13-triggered Cy5 fluorescence recovery of ERMs was tested by fluorescence spectrum analysis and an *in vivo* spectrum imaging system (Fig. 1H). The fluorescence spectra of nERMs remained unchanged before and after incubation with MMP13. In contrast, incubation with MMP13 substantially magnified the Cy5 fluorescence intensity of ERMs due to the effective detachment of Cy5-containing EPs from BHQ3-containing micelles. The result was further confirmed by the fluorescence images where MMP13-treated ERMs emitted more intense fluorescence than the other groups.

The protection of siM13 by ERMs from nuclease degradation was evaluated *via* agarose gel electrophoresis (Fig. 1I). Free siM13 remained stable after 6 h of incubation in nuclease-free water. However, it was completely degraded after only 2 h of incubation in 50 % FBS due to nuclease digestion. In contrast, the bands of siM13s loaded by RMs, ERMs, and nERMs gradually became weak and were still detectable after 6 h of incubation. These results confirmed that the micelle encapsulation facilitated protecting siM13 from nuclease degradation.

3.4. ERMs@siM13 delivery at cellular levels

Diseased chondrocytes highly express MMP13 [15], which are proposed to detach the Cy5-and PEG-containing EPs from the micelles to expose cRGD ligands, achieving diseased chondrocyte-specific uptake and Cy5 fluorescence restoration (Fig. 2A). To test these hypotheses, we first induced diseased chondrocytes by incubating primary chondrocytes with IL-1β [43,44]. MMP13 expression in IL-1β-treated chondrocytes was significantly higher than that in normal chondrocytes, indicating successful generation of diseased chondrocytes (Fig. 2B). Notably, although the highest MMP13 expression was observed for cells incubated for 72 h, cell viability substantially decreased. Hence, the incubation time was set at 48 h for subsequent assay.

First, we investigated whether ERMs could be cleaved by MMP13 secreted by diseased chondrocytes to detach EP by monitoring Cy5 fluorescence restoration. MMP13-inert nERMs emitted weak fluorescence after incubation with normal or diseased chondrocytes for 2 h (Fig. 2C). In contrast, ERMs showed faint fluorescence after incubation with normal chondrocytes. However, after 2 h of incubation with diseased chondrocytes, they exhibited significantly more intense fluorescence. These results confirmed that ERMs could be activated by diseased chondrocyte-secreted MMP13 to release Cy5-containing EP.

Further, we examined whether MMP13-triggered detachment of EPs promoted the micelle uptake by diseased chondrocytes. The flow cytometry assay showed that nERMs@C6 was taken up by the diseased chondrocytes at a low level comparable to cRGD-free Ms@C6 (Fig. 2D). In contrast, cellular internalization of ERMs@C6 was significantly higher than that of nERMs, which was even comparable to cRGD-exposed RMs@C6. A similar trend was also found in the confocal images (Fig. 2E, top). These results suggest that ERMs@C6 uptake by diseased chondrocytes was considerably promoted by MMP13 activation-induced cRGD exposure. Notably, RMs@C6 uptake by normal chondrocytes was higher than ERMs@C6, indicating that EPs protected ERMs from nonspecific uptake by normal chondrocytes (Fig. 2E, bottom).

siRNAs silence target mRNAs in the cytoplasm. Cationic lipids, such as DOTAP, have been reported to promote endosome escape of siRNAs from nanovehicles by destabilizing endosome membranes [26]. Herein, we investigated the intracellular delivery of nERMs@FAM-siRNA by labeling late endosomes/lysosomes with LysoTracker Red. After 1 h of incubation, most FAM-siRNA loaded by ERMs was colocalized with the lysosomes with a colocalization coefficient of 0.60, indicating that ERMs entered cells *via* the endosome-lysosome pathway (Fig. 2F and G). As incubation time prolonged, FAM-siRNAs gradually separated from the lysosomes. In particular, after 8 h of incubation, the colocalization coefficient decreased to 0.27, indicating that siM13 could effectively escape from endosomes.

3.5. Diagnostic and therapeutic effects of ERMs@siM13 on diseased chondrocytes

The diagnostic and therapeutic efficacy of ERMs@siM13 was evaluated by treating diseased chondrocytes with various siM13-containing formulations, followed by diagnosis with ERMs (Fig. 3A and B). PBS-treated diseased chondrocytes emitted significantly higher fluorescence signals than normal chondrocytes, confirming the MMP13-overexpressed status of diseased chondrocytes. The free siM13 and

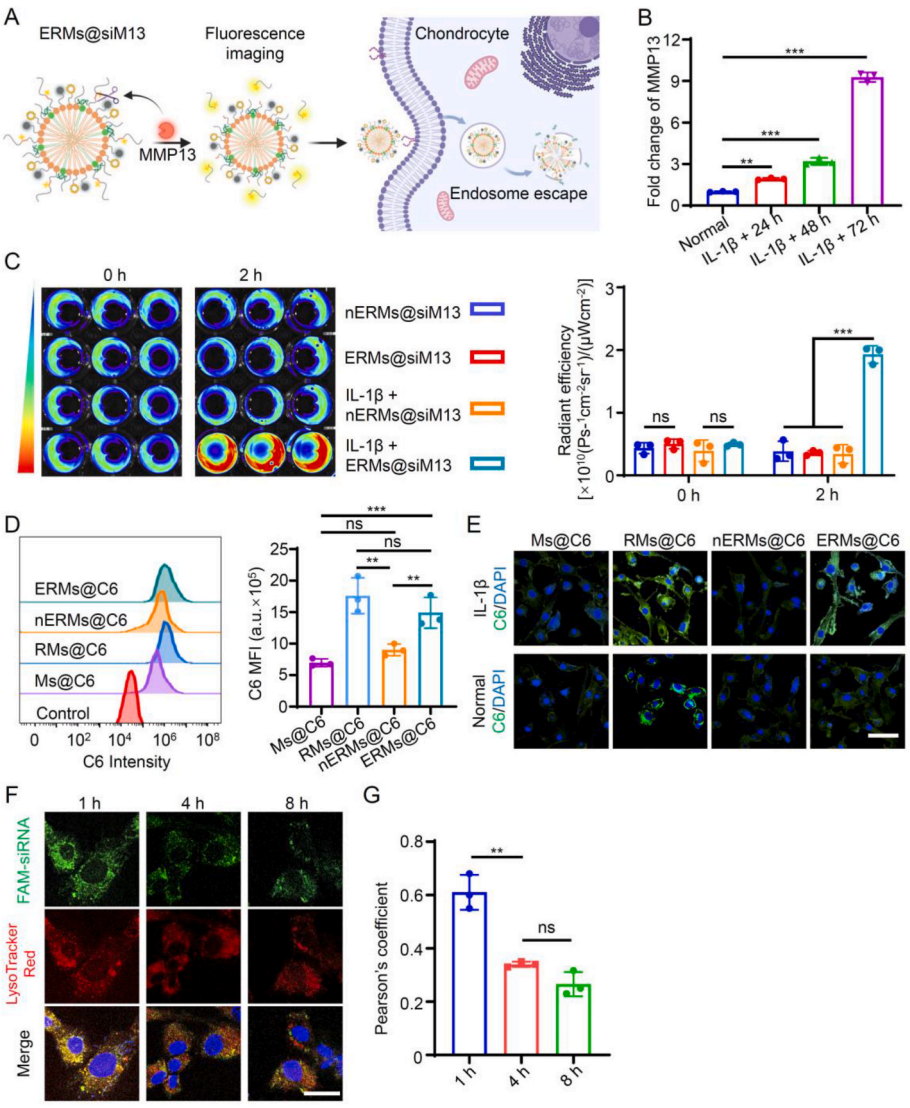

Fig. 2. ERMs@siM13 delivery at cellular levels. (A) Schematic illustration of MMP13-triggered diseased chondrocyte-specific delivery and fluorescence imaging of ERMs@siM13. (B) Fold change of MMP13 expression in culture medium was determined by enzyme-linked immunosorbent assay (ELISA) after chondrocytes were induced by IL-1β for different intervals. (C) Representative fluorescence images and the corresponding fluorescence intensity of normal or diseased chondrocytes after incubation with ERMs or nERMs for 2 h. (D) Representative flow cytometry histogram showing the uptake of coumarin 6 (C6)-labeled micelles by the diseased chondrocytes after 2 h of incubation and the corresponding mean fluorescence intensity (MFI) of C6. (E) Representative confocal images of IL-1β-induced diseased chondrocytes after 2 h of incubation with C6-labeled various micelles. Scale bar: 50 μm. (F) Intracellular delivery of ERMs@FAM-siRNA in IL-1β-induced diseased chondrocytes. Late endosomes/lysosomes are labeled by LysoTracker Red. Scale bar: 25 μm. (G) Pearson's correlation coefficients calculated from Panel F. Data are presented as mean ± SD (n = 3). $^{**}P < 0.01$, $^{***}P < 0.001$, and ns, no significant difference among the marked groups using nonparametric two-tailed analysis of variance.

nERMs@siM13 groups showed strong fluorescence at a level comparable to the PBS control, indicating limited MMP13 downregulation. This result was attributed to their insufficient uptake by the diseased chondrocytes. In contrast, ERMs@siM13 led to faint Cy5 fluorescence comparable to the normal chondrocytes, indicating effective MMP13 downregulation. These results confirmed that ERMs@siM13 could efficiently silence MMP13 and diagnose the therapeutic efficacy at cellular levels.

To further confirm the therapeutic efficacy of ERMs@siM13, we detected *mmp13* mRNA expression *via* RT-qPCR assay after the diseased chondrocytes were treated, as described above (Fig. 3C). The *mmp13* mRNA expression in the PBS control was 15.58-fold higher than normal chondrocytes, showing the MMP13-overactivated abnormality. Treatment with ERMs@siM13 decreased the *mmp13* mRNA expression (23.66 % remaining of the PBS control) to a greater extent than free siM13 and nERMs@siM13 (80.0 % and 54.91 % remaining of the PBS control, respectively) due to the more efficient chondrocyte uptake.

A similar trend was also observed in protein expression of MMP13 by Western blot assay, indicating that silencing *mmp13* mRNA led to MMP13 downregulation (Fig. 3D). Meanwhile, among all treatment groups, ERMs@siM13 upregulated Col 2 at the highest level, even comparable to normal chondrocytes. Moreover, these results were further confirmed by the confocal imaging, where ERMs@siM13 induced MMP13 downregulation and Col 2 upregulation to an extent close to normal chondrocytes (Fig. 3E and F). These results suggest that ERMs@siM13 could downregulate MMP13 protein by silencing *mmp13* mRNA, reducing Col 2 degradation.

Diseased chondrocytes have lower proliferative activity than normal chondrocytes. Herein, we investigated whether treatment with ERMs@siM13 could restore the survivability of diseased chondrocytes *via* EdU staining (Fig. 3G). The EdU-positive cells in the ERMs@siM13 group were 3.45, 2.37, and 2.08-fold of the PBS control, free siM13, and

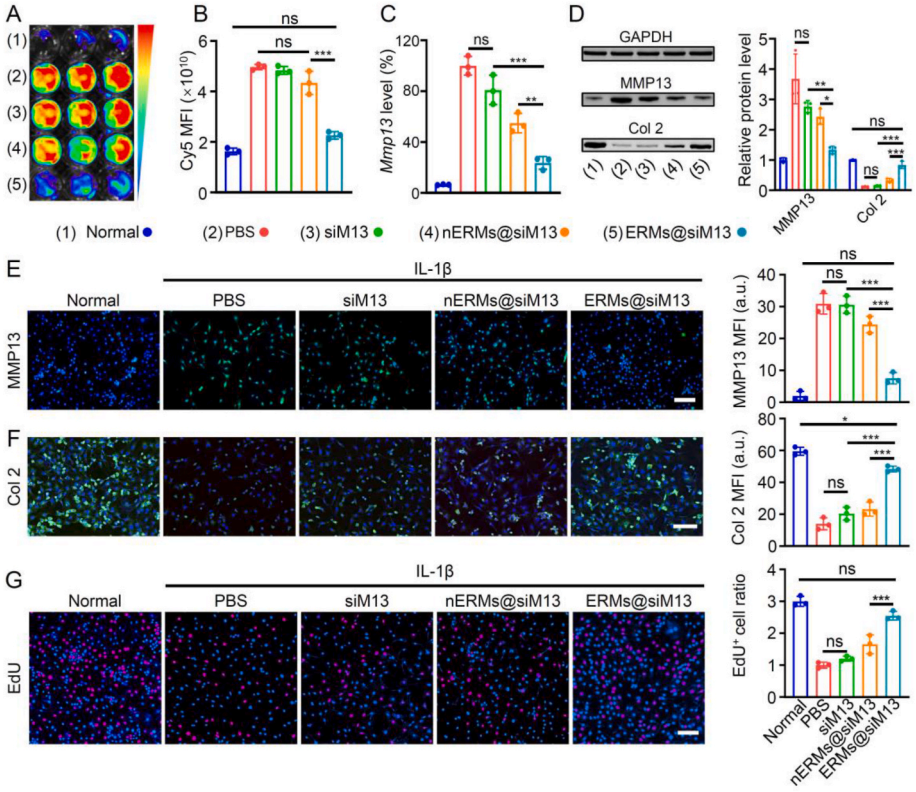

Fig. 3. Diagnostic and therapeutic effects of ERMs@siM13 on diseased chondrocytes. (A) The diseased chondrocytes were treated with the indicated formulations, followed by 2 h of incubation with ERMs to diagnose the chondrocyte status. Normal chondrocytes served as a control. (B) Mean fluorescence intensity (MFI) of Cy5 calculated from Panel (A). (C) *Mmp13* mRNA levels of diseased chondrocytes relative to that of the PBS control after treated with RMs@siM13, nERMs@siM13, and ERMs@siM13. (D) Representative Western blot images showing MMP13, Col 2, and GAPDH protein levels after treatment mentioned above and the corresponding mean protein expression of MMP13 and Col 2. (E–F) Immunofluorescence staining and semiquantitative analysis of (E) MM13 and (F) Col 2 for diseased chondrocytes after treatment mentioned above. (G) Proliferation assay of diseased chondrocytes that were treated as mentioned above, as determined *via* EdU staining. EdU^+ cell ratios relative to the PBS control were calculated. Scale bar: 100 μm. Data are presented as mean ± SD. $^*P < 0.05$, $^{**}P < 0.01$, $^{***}P < 0.001$, and ns, no significant difference among the marked groups using nonparametric two-tailed analysis of variance.

nERMs@siM13 groups, respectively, and were even comparable to normal chondrocytes. These results suggest that ERMs@siM13 could transfer the diseased chondrocytes to a healthier status for enhanced regeneration activity.

3.6. Delivery and diagnostic ability of ERMs@siM13 in the PTOA mice

Intraarticular retention of ERMs@DiR was evaluated after a single-dose injection through *in vivo* fluorescence imaging. The DiR fluorescence in the joints of ERMs@DiR-treated mice declined more slowly over time than that of nERMs@DiR group (Fig. 4A and B). Further quantitative data show that the area under curve (AUC) in the ERMs@DiR group was 1.99-fold significantly higher than that in the nERMs@DiR group (Fig. 4B, $P < 0.001$), indicating prolonged articular retention.

To explore the potential retention mechanism for ERMs, the cartilage distribution of ERMs@C6 at the histological level was examined. Whether ERMs@C6 or nERMs@C6 showed poor distribution in the normal cartilage that expressed MMP13 (red fluorescence) at an extremely low level (Fig. 4C and D). In contrast, ERMs@C6 was extensively perfused in the MMP13-overactivated diseased cartilage, showing 3.15-fold higher fluorescence intensity than nERMs@C6. Moreover, ERMs (green fluorescence) were primarily distributed in the MMP13-rich area. Therefore, the extended retention of ERMs in the diseased cartilage was attributed to their increased internalization by diseased chondrocytes after MMP13-medicated cRGD exposure.

To set an appropriate period for diagnosis, we first detected the Cy5 fluorescence decay in the joints of PTOA mice after a single-dose injection of ERMs or nERMs. The nERMs-treated joints showed weak Cy5 fluorescence all the time. In contrast, Cy5 fluorescence in the ERMs-treated joints peaked at 7 h and gradually declined over time, with the fluorescence intensity falling below 5 % of the maximum value at 72 h (Fig. S6 A-B). These results revealed that the Cy5 fluorescence signal completely washed out 3 days after a single-dose injection of these formulations. Therefore, the diagnosis was performed on day 4 post-treatment. Notably, Cy5 fluorescence decayed from the joints more rapidly than DiR fluorescence. This result occurred because the detached Cy5-containing EP motif had a smaller dimension and thus was more easily eliminated from the joints.

The PTOA mice were treated with ERMs@siM13 and nERMs@siM13 every 5 days for 9 cycles. Then, ERMs were intraarticularly injected on days 17, 32, 42, and 57 post-surgery (i.e., on day 4 posttreatment) for periodic diagnosis when the Cy5 fluorescence signals from the last dose completely decayed. On day 17 post-surgery (i.e., at the initial stage of treatment), the Cy5 fluorescence intensity from ERMs@siM13 and nERMs@siM13 groups was comparable (Fig. 4E and F). As the treatment continued, ERMs@siM13-treated cartilage emitted weaker fluorescence than the nERMs@siM13 group, signifying more effective relief of PTOA by ERMs@siM13.

Then, the cartilage tissues were processed for immunofluorescence staining of MMP13 at each time point of diagnosis to confirm the diagnostic mechanism of ERMs (Fig. 4G and H). Consistently, despite an MMP13 expression comparable to nERMs@siM13 at the initial 2 weeks, as the treatment pursued, ERMs@siM13 downregulated MMP13 expression to a lower degree than nERMs@siM13. These results confirm that ERMs could precisely diagnose the PTOA severity level during

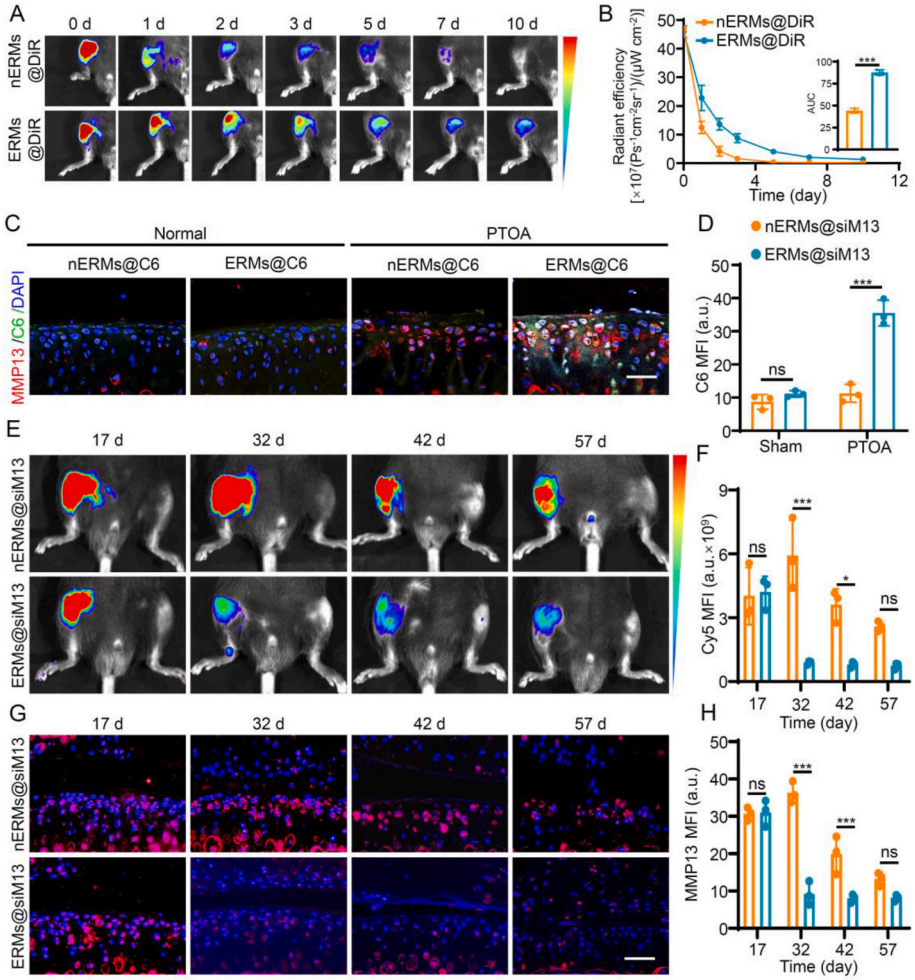

Fig. 4. *In vivo* delivery and diagnostic effects of ERMs@siM13 in the murine posttraumatic osteoarthritis (PTOA) model. (A) Representative fluorescence images of the PTOA mouse joints at various time points after intraarticular injection with ERMs@DiR and nERMs@DiR. (B) The fluorescence signal from Panel (A) was qualified. (C) Representative confocal images showing the ERMs@C6 and nERMs@C6 penetration into healthy and PTOA cartilage. (D) Mean fluorescence intensity (MFI) of C6 calculated from Panel (C). (E) The PTOA mice were treated with ERMs@siM13 and nERMs@siM13 every 5 days for 9 cycles. ERMs were intraarticularly injected at preset time points to monitor the PTOA progression. (F) Cy5 MFI calculated from Panel (E). (G) The PTOA mice were treated as described above. The joints were collected at preset time points and processed for immunofluorescence staining of MMP13. (H) MMP13 MFI calculated from Panel (G). Scale bar: 100 μm. Data are presented as mean ± SD. $^{*}P < 0.05$, $^{***}P < 0.001$, and ns, no significant difference among the marked groups using nonparametric two-tailed analysis of variance.

treatment by responding to dynamically changed MMP13 levels within the diseased cartilage.

3.7. Therapeutic efficacy of ERMs@siM13 in the PTOA mice

The PTOA mice were treated with the siM13-containing formulations every 5 days for 4 or 8 weeks. The H&E staining images revealed that PBS-treated PTOA joints showed severe defects, and the defects enlarged over time, effectively recapitulating the cartilage-damaged status of PTOA (Fig. 5A). Treatment with siM13, Ms@siM13, and nERMs@siM13 retarded the cartilage defects to a limited degree. In contrast, the ERMs@siM13-treated cartilage exhibited a complete morphology after 4 and 8 weeks of treatment, almost comparable to the sham group, indicating favorable efficacy.

Further, the safranin O/fast green staining was performed to observe the cartilage morphology. Compared to the sham group, the PBS group showed typical morphological changes of OA, i.e., increased cartilage loss (safranin O-labeling area), which persistently deteriorated over time (Fig. 5B). Cartilage morphological improvement, such as increased proteoglycan retention, was observed in the siM13, RMs@siM13, nERMs@siM13, and ERMs@siM13 groups after 4 and 8 weeks of treatment. In particular, ERMs@siM13 treatment led to the most integral cartilage morphology and reduced Mankin score (Fig. 5C) to a comparable degree (4 w: 11.70 %; 8 w: 20.73 %) to the sham group (4 w: 2.56 %; 8 w: 4.88 %). These findings suggest that ERMs@siM13 could effectively prevent cartilage degeneration by downregulating MMP13 expression.

Osteophyte formation increased during OA progression to stabilize the damaged OA joints [45]. Among all treatment groups, the ERMs@siM13-treated joints had the lowest number of osteophytes (Fig. 5D and E). These results suggest that ERMs@siM13 could maintain healthy bone morphology by retarding OA progression.

3.8. Therapeutical mechanism study of ERMs@siM13 via immunohistochemical (IHC) assay

Considering the inspiring efficacy of ERMs@siM13 in the PTOA mice, we further explored its therapeutic mechanism through IHC staining. The PBS-treated cartilage expressed 20.24- and 15.24-fold higher MMP13 than the sham group at weeks 4 and 8, respectively, persistently maintaining the MMP13-overactivated feature of PTOA (Fig. 6A and B). Among all treatment groups, MMP13 was

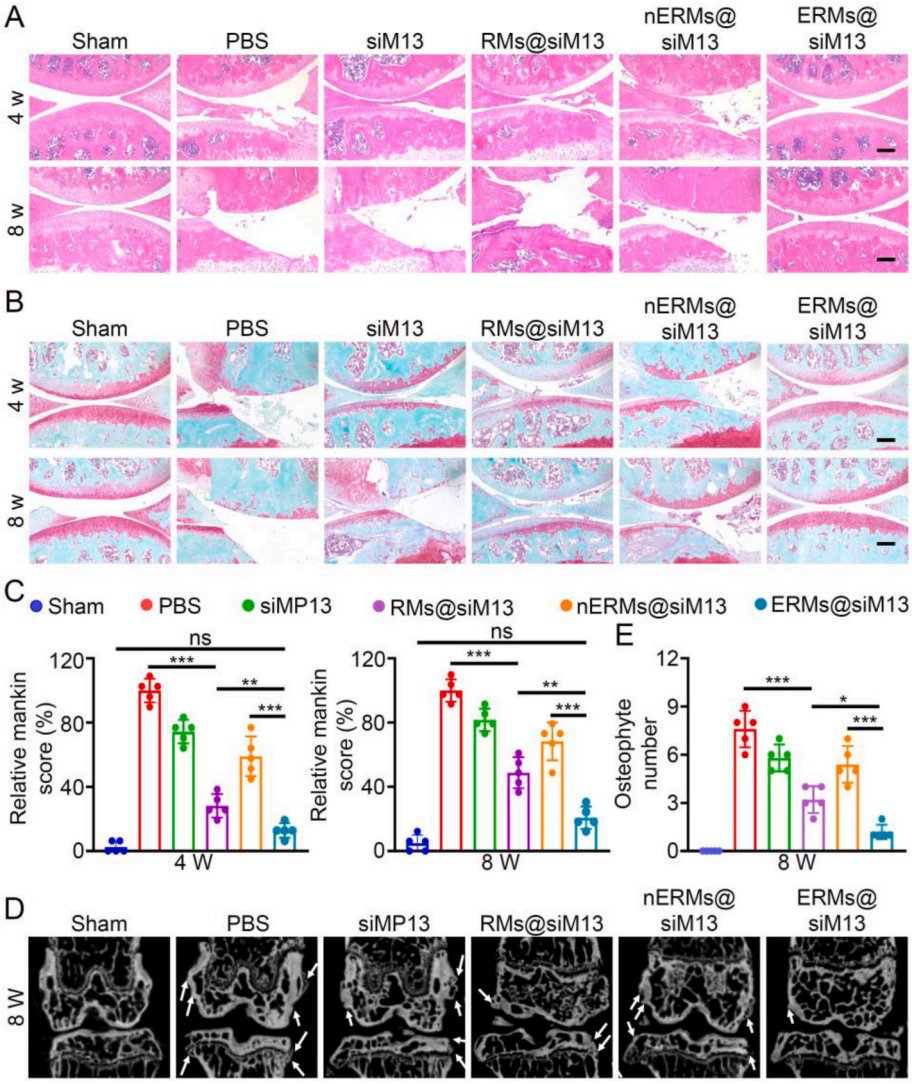

Fig. 5. Therapeutic efficacy of ERMs@siM13 in the posttraumatic osteoarthritis (PTOA) mice. (A) Representative hematoxylin and eosin (H&E) staining images of articular cartilage at weeks 4 and 8 after treatment with the indicated formulations. (B) Representative safranin O/fast green staining images of articular cartilage after 4 or 8 weeks of treatment. (C) The OA severity at weeks 4 and 8 from Panel (B) was accessed using the Mankin score. (D) Osteophyte (white arrows) formation at week 8 posttreatment was examined through micro-computed tomography (Micro-CT). (E) The osteophyte number was quantified from Panel (D). Scale bar: 200 μm. Data are presented as mean ± SD. $^{*}P < 0.05$, $^{**}P < 0.01$, $^{***}P < 0.001$, and ns, no significant difference among the marked groups using nonparametric two-tailed analysis of variance.

downregulated after 4 and 8 weeks of treatment following the sequence: ERPs@siM13 > RMs@siM13 > nERMs@siM13 > siM13.

Col 2 is the primary matrix skeleton of cartilage tissues and is primarily degraded by MMP13 [8,12]. After 4 and 8 weeks of treatment, corresponding to the MMP13 downregulation trend, a synchronous upregulation in Col 2 levels was observed (Fig. 6C and D). In particular, ERMs@siM13-treated cartilage showed 4.06- and 6.04-fold higher Col 2 expression than the PBS control, suggesting the most effective blockade of Col 2 digestion. These results support that the favorable efficacy of ERMs@siM13 was attributed to its ability to silence MMP13 protein, thereby improving the Col 2 turnover in the cartilage tissues.

In addition, treatment with the siM13-containing formulations also enhanced ACAN turnover to different degrees, positively associated with their downregulation levels of MMP13 (Fig. 6E and F). In particular, ERMs@siM13 led to 4.92- and 8.36-fold higher ACAN expression than the PBS control at weeks 4 and 8, respectively, indicating the most effective relief of ACAN degradation. These results were attributed to two reasons. First, although ACAN is degraded primarily by a disintegrin and metalloproteinase with thrombospondin motifs 5 (ADAMTS-5), MMP13 also digests ACAN [46–48]. Moreover, upon MMP13 cleavage, the newly produced fragments with smaller sizes more easily perfuse through the cartilage matrix to reach ADAMTS-5 for degradation. Second, the MMP13-induced breakdown of the collagen network makes ADAMTS-5 more accessible to its substrate ACAN [46–48]. Overall, MMP13 downregulation increased ACAN turnover primarily by reducing the substrate availability to ADAMTS-5.

3.9. Biosafety evaluation

Considering the intraarticular administration route, we first investigated the synovium irritation of ERMs@siM13 by injecting single-dose formulations into the joints of healthy mice (Fig. 7A). The H&E staining images of synovium showed that no infiltration of immune cells occurred for all treatment groups, indicating their negligible synovium irritation.

The PTOA mice were treated every 5 days for 8 weeks. The H&E staining images of the major organs collected at the end of treatment revealed no morphological abnormity, indicating that these

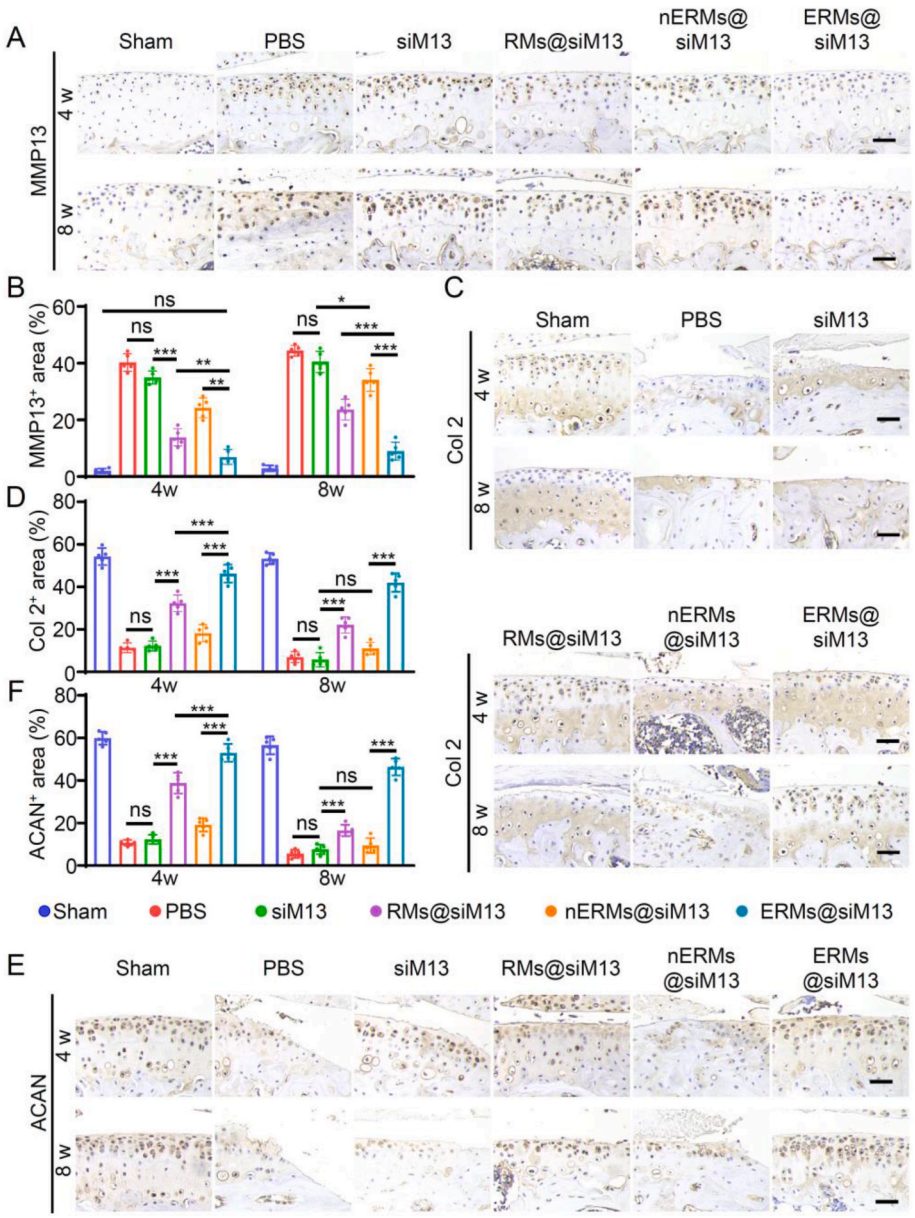

Fig. 6. Immunohistochemical (IHC) staining of sham or posttraumatic osteoarthritis (PTOA) mouse knee joints after 4 and 8 weeks of treatment. (A) Representative IHC staining images of MMP13 in the mouse cartilages after treatment with the indicated formulations. The sham group served as a normal control. (B) The MMP13-positive ($MMP13^+$) area (%) calculated from Panel (A). (C) Representative IHC staining images of Col 2 in the mouse cartilages posttreatment with the indicated formulations. (D) The Col 2-positive ($Col\ 2^+$) area calculated from Panel (C). (E) Representative IHC staining images of aggrecan (ACAN) in the mouse cartilages posttreatment with the indicated formulations. (F) The ACAN-positive ($ACAN^+$) area calculated from Panel (E). Scale bar: 100 μm. Data are presented as mean ± SD. $^*P < 0.05$, $^{**}P < 0.01$, $^{***}P < 0.001$, and ns, no significant difference among the marked groups using nonparametric two-tailed analysis of variance.

formulations had no discernible organ toxicities (Fig. 7B). In addition, the indexes from the routine blood examination and blood biochemical analysis fell within the normal range (Fig. S7). Therefore, these data support that ERMs@siM13 and other formulations had negligible toxicities to the major organs and blood after local intraarticular injection.

4. Discussion

The post-synthesis method is extensively used to conjugate ligands on the nanoparticle surface. However, this approach can not precisely and reproducibly control the ligand proportion, particularly in the presence of multiple ligands. Therefore, for the micelle assembly, we first synthesized a series of lipid-tethered ligands, including DSPE-PEG_{2000}-EP (nEP), DSPE-PEG_{2000}-cRGD, and DSPE-PEG_{2000}-BHQ3. As such, each ligand ratio in the micelle formulation can be flexibly adjusted by changing its feeding amount to optimize the micelle's diagnostic and therapeutic efficacy.

The fluorescence dye (donor) can be efficiently quenched by the BHQ3 (acceptor) within a distance of 10 nm *via* forster resonance energy transfer (FRET) [18]. Accordingly, in the previous studies, the dyes are generally linked to BHQ3 *via* a short disease-specific stimulus-cleavable linker for diagnosis [18,49]. However, this connection approach limits the probe assembly into nanovehicles. Herein, we independently synthesized lipid-tethered DSPE-PEG_{2000}-EP and DSPE-PEG_{2000}-BHQ3, which could be easily fabricated into the micelles *via* the facile thin-film hydration method (Scheme 1A). More importantly, unlike the previous connection approach (i.e., the ratio is fixed at 1:1), the ratio of BHQ3 versus Cy5 was tunable. In particular, when the molar ratio of BHQ3 versus Cy5 was increased from 1:1 to 1:2, the quenching efficiency of Cy5 fluorescence was further elevated (Fig. 1F). Hence, ERMs showed a

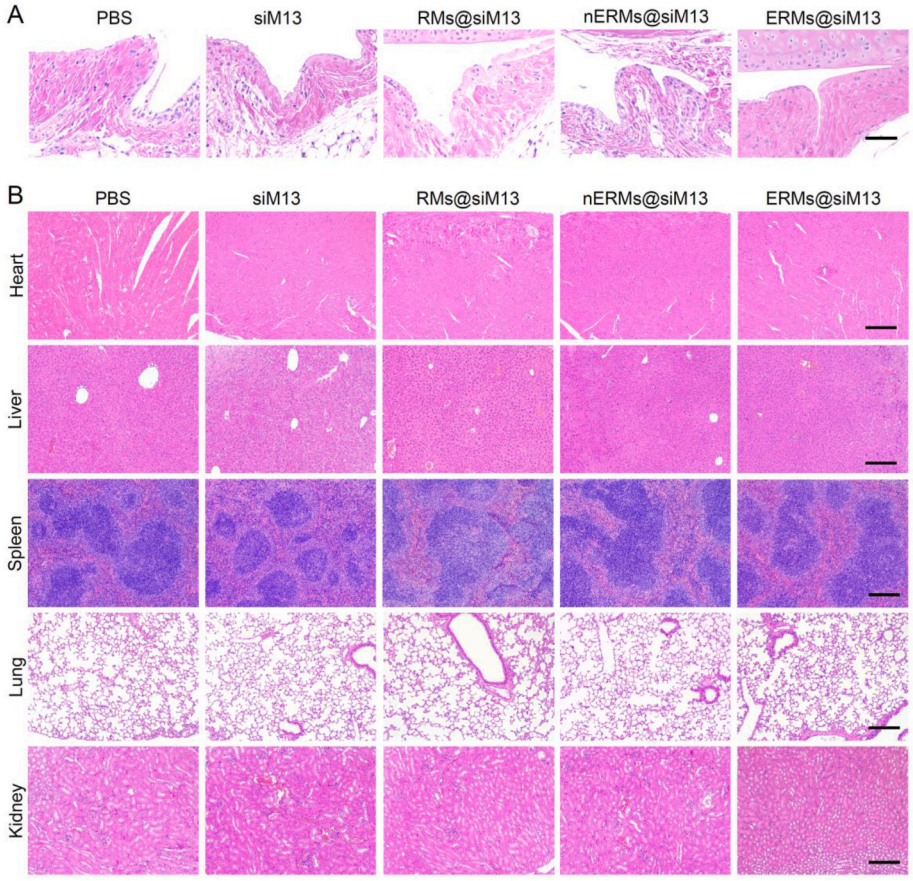

Fig. 7. Biosafety assessment of ERMs@siM13. (A) Representative hematoxylin-eosin (H&E) staining images of the knee joint synovium of healthy mice on the 5th day after intraarticular injection with the single-dose indicated formulations. Scale bar: 100 μm. (B) Representative H&E staining images of the major organs of the posttraumatic osteoarthritis (PTOA) mice after treatment with the indicated formulations every 5 days for 8 weeks. Scale bar: 200 μm.

high signal-to-noise ratio when detecting diseased chondrocytes in vitro (5.37) and *in vivo* (8.97) (Fig. 2C & Fig. S6). In addition, the Cy5 fluorescence signal completely decayed at 72 h postinjection because the detached Cy5-containing EP fragments with a small size are easily cleared from the cartilage tissues (Fig. S6). This property allows periodic diagnosis without the last-dose interference. With this subtle design, ERMs@siM13 could diagnose the OA progression during treatment at cellular levels and in the murine PTOA model (Fig. 3A and B & Fig. 4E and F).

siRNAs can inhibit MMP13 more specifically than small-molecule inhibitors. However, it is difficult for free siRNAs to enter diseased chondrocytes at sufficient concentrations due to multiple barriers, such as nuclease degradation and less effective cell uptake. The cationic lipid DOTAP-containing micelle had a high EE for siM13 (approximately 90 %) *via* electrostatic adsorption when the N/P ratio was over 6:1 (Table S1). In addition, encapsulation within the micelle effectively protected siM13 from nuclease degradation, as indicated by agarose gel electrophoresis analysis (Fig. 1I).

Normal and diseased chondrocytes express αvβ3 integrins [27,28], mediating cRGD-modified nanovehicles' internalization [29–31]. However, surrounding the MMP13-deficient healthy chondrocytes, the ERMs' cRGD ligands were shielded by EP-derived PEG layer, showing significantly lower cellular uptake than cRGD-exposed RMs (Fig. 2E, bottom). In contrast, in the MMP13-overexpressed diseased chondrocytes, the PEG-containing EPs were detached from the micelle by MMP13 cleavage, leading to cRGD exposure. Therefore, ERMs showed a comparable uptake by diseased chondrocytes to cRGD-exposed RMs (Fig. 2D and E, top). Diseased chondrocyte-specific uptake of ERMs was further confirmed in the *in vivo* experiments, where ERMs selectively accumulated to MMP13-overexpressed area (i.e., diseased chondrocytes) (Fig. 4C). Moreover, this increased cell uptake markedly prolonged articular retention of ERMs, which had a 1.99-fold higher AUC than its MMP13-insensitive counterpart (nERMs) (Fig. 4A and B). In addition, ERMs@siM13 promoted the endosome escape of siM13 by destabilizing the endosome membrane with the cationic lipid (DOTAP) (Fig. 2F).

By efficiently delivering siM13 to diseased chondrocytes, ERMs@siM13 substantially downregulated MMP13 expression and thus increased Col 2 turnover in the cartilage tissue of the PTOA mice (Fig. 6A–D). ACAN is primarily degraded by ADAMTS-5 [46–48]. Unexpectedly, treatment with ERMs@siM13 simultaneously elevated ACAN turnover (Fig. 6E and F). This result occurred mainly because MMP13 downregulation made the substrate less accessible to its enzyme, as discussed above. In addition to increasing cartilage matrix turnover, ERMs@siM13 enhanced chondrocyte proliferation by downregulating MMP13, confirming its ability to promote cartilage regeneration (Fig. 3G). Therefore, ERMs@siM13 effectively retarded cartilage degeneration after 4 and 8 weeks of treatment, as indicated by the H&E and safranin O/fast green staining (Fig. 5A–C). Moreover, the lowest number of osteophytes formed in the ERMs@siM13-treated joints, indicating that it facilitated healthy bone morphology by delaying OA progression (Fig. 5D and E). In addition, ERMs@siM13 exerted negligible synovium irritation after a single-dose injection while causing no detectable organ and blood toxicities after 8 weeks of treatment (Fig. 7A–B & Fig. S7).

Currently, OA is diagnosed primarily through patient-reported symptoms and X-ray imaging [6]. Unfortunately, X-ray imaging fails to detect subtle alterations in early-stage disease [7]. In contrast,

fluorescence imaging may diagnose early-stage OA by detecting specific proteins and biological processes involved in OA progression. However, the fluorescent probe is delivered into the diseased cartilage area primarily through an invasive approach, i.e., intraarticular injection. Therefore, frequent injections bring pain to patients. Herein, the integrated diagnosis and treatment micelle ERMs@siM13 retained in the articular joints for over 10 days (Fig. 4A and B) and thus could be administered in a long interval, thereby facilitating improved patients' compliance.

5. Conclusion

In the current study, an integrated diagnosis and treatment micelle, ERMs@siM13, was developed to diagnose and intervene early-stage PTOA by targeting the overexpressed MMP13 in the diseased cartilage tissues. In MMP13-deficient normal cartilage, ERMs@siM13 maintained a fluorescence-quenched status for low background noise and avoided nonspecific cell uptake due to the cRGD ligands shielded by PEG-containing EPs. In contrast, upon reaching the diseased chondrocytes, the overexpressed MMP13 could detach the PEG shell, restoring Cy5 fluorescence for early-stage OA diagnosis and exposing cRGD ligands for increased cellular internalization and on-demand treatment (i.e., MMP13 downregulation). Accordingly, ERMs@siM13 effectively retarded the early-stage OA progression by restoring the balance of cartilage matrix metabolism. Moreover, ERMs@siM13 can provide a real-time report about the OA progression degree by promptly responding to different levels of MMP13, which reflects the PTOA severity. Finally, ERMs@siM13 realized effective diagnosis and timely intervention for the early-stage PTOA in the murine PTOA model without causing additional side effects, which warrants further exploration in the clinical application in the future.

Ethics approval and consent to participate

Male C57 mice (6–7 weeks old) were purchased from Changzhou Cavens Experimental Animal Co., Ltd. (Jiangsu, China). The mice were kept at 20–25 °C and 50 % humidity with a 12 h light/dark cycle. They were provided with unrestricted access to water and rodent chow. All animal experiments were performed following the protocols approved by the ethics committee of Shanghai University (NO. ECSHU 2023–101).

CRediT authorship contribution statement

Dongyang Zhou: Writing – original draft, Methodology, Investigation, Formal analysis, Data curation, Conceptualization. **Yan Wei:** Writing – review & editing, Visualization, Conceptualization, Supervision, Funding acquisition. **Shihao Sheng:** Methodology, Investigation, Formal analysis. **Miaomiao Wang:** Methodology, Investigation, Formal analysis. **Jiajing Lv:** Validation, Software. **Bowen Zhao:** Validation, Software. **Xiao Chen:** Validation, Supervision, Conceptualization. **Ke Xu:** Validation, Supervision, Conceptualization. **Long Bai:** Methodology, Conceptualization. **Yan Wu:** Methodology. **Peiran Song:** Methodology, Conceptualization. **Fengjin Zhou:** Review & editing, Visualization, Conceptualization. **Hao Zhang:** Writing-review & editing, Supervision, Resources, Conceptualization. **Zhongmin Shi:** Writing-review & editing, Supervision, Resources, Conceptualization. **Jiacan Su:** Writing-review & editing, Supervision, Resources, Funding acquisition, Conceptualization.

Declaration of competing interest

All authors declare that there are no competing interests.

Acknowledgments

This work was supported by Integrated Project of Major Research Plan of National Natural Science Foundation of China (92249303), National Natural Science Foundation of China (82230071, 82172098, 82371603, 82102217, 81872428, and 81703010), the Shanghai Rising Star Program (21QA1412000), Shanghai Hospital Development Center (SHDC2023CRT013), Shanghai Committee of Science and Technology (23141900600, Laboratory Animal Research Project), Shanghai Baoshan District Medical Health Project (21-E-14), the Construction of Key Medical Disciplines of Baoshan District of Shanghai (BSZK-2023-Z07), the Shanghai Municipal Natural Science Foundation (23ZR1463300), Postdoctoral Fellowship Program of CPSF (GZB20230397), and General Funding for China Postdoctoral Science Foundation (2023M732179).

Appendix A. Supplementary data

Supplementary data to this article can be found online at https://doi.org/10.1016/j.bioactmat.2024.04.010.

References

[1] S.K. Bedingfield, J.M. Colazo, F. Yu, D.D. Liu, M.A. Jackson, L.E. Himmel, H. Cho, L.J. Crofford, K.A. Hasty, C.L. Duvall, Amelioration of post-traumatic osteoarthritis via nanoparticle depots delivering small interfering RNA to damaged cartilage, Nat. Biomed. Eng. 5 (9) (2021) 1069–1083, https://doi.org/10.1038/s41551-021-00780-3.

[2] C.R. Maia, R.F. Annichino, M. de Azevedo E Souza Munhoz, E.G. Machado, E. Marchi, M.C. Castano-Betancourt, Post-traumatic osteoarthritis: the worst associated injuries and differences in patients' profile when compared with primary osteoarthritis, BMC Muscoskel. Disord. 24 (1) (2023), https://doi.org/10.1186/s12891-023-06663-9.

[3] Y. Jiang, J. Li, X. Xue, Z. Yin, K. Xu, J. Su, Engineered extracellular vesicles for bone therapy, Nano Today 44 (2022) 101487, https://doi.org/10.1016/j.nantod.2022.101487.

[4] S.K. Bedingfield, J.M. Colazo, M. Di Francesco, F. Yu, D.D. Liu, V. Di Francesco, L. E. Himmel, M.K. Gupta, H. Cho, K.A. Hasty, P. Decuzzi, C.L. Duvall, Top-down fabricated microPlates for prolonged, intra-articular matrix metalloproteinase 13 siRNA nanocarrier delivery to reduce post-traumatic osteoarthritis, ACS Nano 15 (9) (2021) 14475–14491, https://doi.org/10.1021/acsnano.1c04005.

[5] J. Li, H. Zhang, Y. Han, Y. Hu, Z. Geng, J. Su, Targeted and responsive biomaterials in osteoarthritis, Theranostics 13 (3) (2023) 931–954, https://doi.org/10.7150/thno.78639.

[6] A. Brahim, R. Jennane, R. Riad, T. Janvier, L. Khedher, H. Toumi, E. Lespessailles, A decision support tool for early detection of knee OsteoArthritis using X-ray imaging and machine learning: data from the OsteoArthritis Initiative, Comput. Med. Imag. Graph. 73 (2019) 11–18, https://doi.org/10.1016/j.compmedimag.2019.01.007.

[7] D. Hayashi, F.W. Roemer, M. Jarraya, A. Guermazi, Imaging in osteoarthritis, Radiol. Clin. 55 (5) (2017) 1085–1102, https://doi.org/10.1016/j.rcl.2017.04.012.

[8] D.H.A.T. Saxne, The role of the cartilage matrix in osteoarthritis, Nat. Rev. Rheumatol. 7 (1) (2011) 50–56, https://doi.org/10.1038/nrrheum.2010.198.

[9] H. Zhang, L. Wang, J. Cui, S. Wang, Y. Han, H. Shao, C. Wang, Y. Hu, X. Li, Q. Zhou, J. Guo, X. Zhuang, S. Sheng, T. Zhang, D. Zhou, J. Chen, F. Wang, Q. Gao, Y. Jing, X. Chen, J. Su, Maintaining hypoxia environment of subchondral bone alleviates osteoarthritis progression, Sci. Adv. 9 (14) (2023) eabo7868, https://doi.org/10.1126/sciadv.abo7868.

[10] M.B. Goldring, K.B. Marcu, Epigenomic and microRNA-mediated regulation in cartilage development, homeostasis, and osteoarthritis, Trends Mol. Med. 18 (2) (2012) 109–118, https://doi.org/10.1016/j.molmed.2011.11.005.

[11] D. Zhou, F. Zhou, S. Sheng, Y. Wei, X. Chen, J. Su, Intra-articular nanodrug delivery strategies for treating osteoarthritis, Drug Discov. Today 28 (3) (2023) 103482, https://doi.org/10.1016/j.drudis.2022.103482.

[12] M.B. Goldring, The role of the chondrocyte in osteoarthritis, Arthritis Rheumatol. 43 (9) (2000) 1916–1926, https://doi.org/10.1002/1529-0131(200009)43:9<1916::AID-ANR2>3.0.CO, 2-I.

[13] H. Li, D. Wang, Y. Yuan, J. Min, New insights on the MMP-13 regulatory network in the pathogenesis of early osteoarthritis, Arthritis Res. Ther. 19 (1) (2017) 248, https://doi.org/10.1186/s13075-017-1454-2.

[14] Q. Hu, M. Ecker, Overview of MMP-13 as a promising target for the treatment of osteoarthritis, Int. J. Mol. Sci. 22 (4) (2021) 1742, https://doi.org/10.3390/ijms22041742.

[15] M. Wang, E.R. Sampson, H. Jin, J. Li, Q.H. Ke, H. Im, D. Chen, MMP13 is a critical target gene during the progression of osteoarthritis, Arthritis Res. Ther. 15 (1) (2013) R5, https://doi.org/10.1186/ar4133.

[16] M. Koller, S. Qiu, M.D. Linssen, L. Jansen, W. Kelder, J. de Vries, I. Kruithof, G. Zhang, D.J. Robinson, W.B. Nagengast, A. Jorritsma-Smit, B. van der Vegt, G. M. van Dam, Implementation and benchmarking of a novel analytical framework to clinically evaluate tumor-specific fluorescent tracers, Nat. Commun. 9 (1) (2018), https://doi.org/10.1038/s41467-018-05727-y.

[17] J. Mieog, F.B. Achterberg, A. Zlitni, M. Hutteman, J. Burggraaf, R.J. Swijnenburg, S. Gioux, A.L. Vahrmeijer, Fundamentals and developments in fluorescence-guided cancer surgery, Nat. Rev. Clin. Oncol. 19 (1) (2022) 9–22, https://doi.org/10.1038/s41571-021-00548-3.

[18] K. Kiyose, K. Hanaoka, D. Oushiki, T. Nakamura, M. Kajimura, M. Suematsu, H. Nishimatsu, T. Yamane, T. Terai, Y. Hirata, T. Nagano, Hypoxia-sensitive fluorescent probes forin vivo real-time fluorescence imaging of acute ischemia, J. Am. Chem. Soc. 132 (45) (2010) 15846–15848, https://doi.org/10.1021/ja105937q.

[19] T. Myochin, K. Hanaoka, T. Komatsu, T. Terai, T. Nagano, Design strategy for a near-infrared fluorescence probe for matrix metalloproteinase utilizing highly cell permeable boron dipyrromethene, J. Am. Chem. Soc. 134 (33) (2012) 13730–13737, https://doi.org/10.1021/ja303931b.

[20] Z.Q.J.Z. Haimin Chena, L.Z. Chuanbin Mao, Cartilage-targeting and dual MMP-13/pH responsive theranostic nanoprobes for osteoarthritis imaging and precision therapy, Biomaterials 225 (2019) 119520, https://doi.org/10.1016/j.biomaterials.2019.119520.

[21] M.B. Mueller, R.S. Tuan, Anabolic/Catabolic balance in pathogenesis of osteoarthritis: identifying molecular targets, PM&R 3 (6 Suppl 1) (2011) S3–S11, https://doi.org/10.1016/j.pmrj.2011.05.009.

[22] P. Krzeski, C. Buckland-Wright, G. Bálint, G.A. Cline, K. Stoner, R. Lyon, J. Beary, W.S. Aronstein, T.D. Spector, Development of musculoskeletal toxicity without clear benefit after administration of PG-116800, a matrix metalloproteinase inhibitor, to patients with knee osteoarthritis: a randomized, 12-month, double-blind, placebo-controlled study, Arthritis Res. Ther. 9 (5) (2007) R109, https://doi.org/10.1186/ar2315.

[23] J.R. Molina, J.M. Reid, C. Erlichman, J.A. Sloan, A. Furth, S.L. Safgren, C.D. Lathia, S.R. Alberts, A phase I and pharmacokinetic study of the selective, non-peptidic inhibitor of matrix metalloproteinase BAY 12-9566 in combination with etoposide and carboplatin, Anti Cancer Drugs 16 (9) (2005) 997–1002, https://doi.org/10.1097/01.cad.0000176504.86551.5c.

[24] H. Liu, H. Zhang, S. Wang, J. Cui, W. Weng, X. Liu, H. Tang, Y. Hu, X. Li, K. Zhang, F. Zhou, Y. Jing, J. Su, Bone-targeted bioengineered bacterial extracellular vesicles delivering siRNA to ameliorate osteoporosis, Compos. B Eng. 255 (2023) 110610, https://doi.org/10.1016/j.compositesb.2023.110610.

[25] Y. Hu, X. Li, Q. Zhang, Z. Gu, Y. Luo, J. Guo, X. Wang, Y. Jing, X. Chen, J. Su, Exosome-guided bone targeted delivery of Antagomir-188 as an anabolic therapy for bone loss, Bioact. Mater. 6 (9) (2021) 2905–2913.

[26] J. Yan, H. Zhang, G. Li, J. Su, Y. Wei, C. Xu, Lipid nanovehicles overcome barriers to systemic RNA delivery: lipid components, fabrication methods, and rational design, Acta Pharm. Sin. B 14 (2) (2024) 579–601, https://doi.org/10.1016/j.bioactmat.2021.02.014.

[27] Q. Wang, K. Onuma, C. Liu, H. Wong, M.S. Bloom, E.E. Elliott, R.R. Cao, N. Hu, N. Lingampalli, O. Sharpe, X. Zhao, D.H. Sohn, C.M. Lepus, J. Sokolove, R. Mao, C. T. Cisar, H. Raghu, C.R. Chu, N.J. Giori, S.B. Willingham, S.S. Prohaska, Z. Cheng, I.L. Weissman, W.H. Robinson, Dysregulated integrin alphaVbeta3 and CD47 signaling promotes joint inflammation, cartilage breakdown, and progression of osteoarthritis, JCI Insight 4 (18) (2019), https://doi.org/10.1172/jci.insight.128616.

[28] F. Song, X. Mao, J. Dai, B. Shan, Z. Zhou, Y. Kang, Integrin alphaVbeta3 signaling in the progression of osteoarthritis induced by excessive mechanical stress, Inflammation 46 (2) (2023) 739–751, https://doi.org/10.1007/s10753-022-01770-6.

[29] E.A. Murphy, B.K. Majeti, L.A. Barnes, M. Makale, S.M. Weis, K. Lutu-Fuga, W. Wrasidlo, D.A. Cheresh, Nanoparticle-mediated drug delivery to tumor vasculature suppresses metastasis, Proc. Natl. Acad. Sci. U.S.A. 105 (27) (2008) 9343–9348, https://doi.org/10.1073/pnas.0803728105.

[30] N. Duan, J. Li, S. Song, F. Wang, Y. Yang, D. Nie, C. Wang, Y. Sheng, Y. Tao, J. Gao, C. Xu, Y. Wei, Y. Gan, Enzyme-activated prodrug-based smart liposomes specifically enhance tumor hemoperfusion with efficient drug delivery to pancreatic cancer cells and stellate cells, Adv. Funct. Mater. (2021) 2100605, https://doi.org/10.1002/adfm.202100605.

[31] Y. Wei, S. Song, N. Duan, F. Wang, Y. Wang, Y. Yang, C. Peng, J. Li, D. Nie, X. Zhang, S. Guo, C. Zhu, M. Yu, Y. Gan, MT1-MMP-Activated liposomes to improve tumor blood perfusion and drug delivery for enhanced pancreatic cancer therapy, Adv. Sci. (2020) 1902746, https://doi.org/10.1002/advs.201902746.

[32] L. Zhu, P. Kate, V.P. Torchilin, Matrix metalloprotease 2-responsive multifunctional liposomal nanocarrier for enhanced tumor targeting, ACS Nano 6 (4) (2012) 3491–3498, https://doi.org/10.1021/nn300524f.

[33] J. Wang, X. Li, S. Wang, J. Cui, X. Ren, J. Su, Bone-targeted exosomes: strategies and applications, Adv. Healthcare Mater. 12 (18) (2023), https://doi.org/10.1002/adhm.202203361.

[34] Y. Tao, Y. Chen, S. Wang, W. Chen, D. Zhou, D. Chen, C. Zhang, Z. Wu, J. Yan, H. Zhang, Y. Wei, J. Su, Optimizing the modification density of acid oligopeptides to enhance the bone-targeting activity of liposomes, Compos. B Eng. 247 (2022) 110288, https://doi.org/10.1016/j.compositesb.2022.110288.

[35] J. Yan, M. Wang, S. Lv, D. Chen, Z. Wu, D. Zhou, S. Zhang, J. Lv, K. Xu, C. Xu, Y. Wei, SiATG5-loaded cancer cell membrane-fused liposomes induced increased uptake of albumin-bound chemotherapeutics by pancreatic cancer cells, J. Contr. Release 367 (2024) 620–636, https://doi.org/10.1016/j.jconrel.2024.01.055.

[36] S.Y.Y.Q. Jinjin Zhu, Y.H.Z.Z. Panyang Shen, A.G.M.X. Shuying Shen, Stem cell-homing hydrogel-based miR-29b-5p delivery promotes cartilage regeneration by suppressing senescence in an osteoarthritis rat model, Sci. Adv. 8 (2022) eabk0011, https://doi.org/10.1126/sciadv.abk0011.

[37] K.P.H. Pritzker, S. Gay, S.A. Jimenez, K. Ostergaard, J.P. Pelletier, P.A. Revell, D. Salter, W.B. van den Berg, Osteoarthritis cartilage histopathology: grading and staging, Osteoarthritis Cartilage 14 (1) (2006) 13–29, https://doi.org/10.1016/j.joca.2005.07.014.

[38] T. Aigner, J.L. Cook, N. Gerwin, S.S. Glasson, S. Laverty, C.B. Little, W. McIlwraith, V.B. Kraus, Histopathology atlas of animal model systems-overview of guiding principles, Osteoarthritis Cartilage 18 (2010) S2–S6, https://doi.org/10.1016/j.joca.2010.07.013.

[39] H. Chen, H. Paholak, M. Ito, K. Sansanaphongpricha, W. Qian, Y. Che, D. Sun, 'Living' PEGylation on gold nanoparticles to optimize cancer cell uptake by controlling targeting ligand and charge densities, Nanotechnology 24 (35) (2013) 355101, https://doi.org/10.1088/0957-4484/24/35/355101.

[40] G. Su, H. Jiang, B. Xu, Y. Yu, X. Chen, Effects of protein corona on active and passive targeting of cyclic RGD peptide-functionalized PEGylation nanoparticles, Mol. Pharm. 15 (11) (2018) 5019–5030, https://doi.org/10.1021/acs.molpharmaceut.8b00612.

[41] X. Shao, P. Schnau, W. Qian, X. Wang, Quantitatively understanding cellular uptake of gold nanoparticles via radioactivity analysis, J. Nanosci. Nanotechnol. 15 (5) (2015) 3834, https://doi.org/10.1166/jnn.2015.9486.

[42] B.K. Liebov, A.D. Arroyo, N.I. Rubtsova, S.A. Osharovich, E.J. Delikatny, A. V. Popov, Nonprotecting group synthesis of a phospholipase C activatable probe with an azo-free quencher, ACS Omega 3 (6) (2018) 6867–6873, https://doi.org/10.1021/acsomega.8b00635.

[43] P. Hu, F. Sun, L. Jiang, J. Bao, L. Wu, Paeoniflorin inhibits IL-1β-induced MMP secretion via the NF-κB pathway in chondrocytes, Exp. Ther. Med. 16 (2) (2018) 1513–1519, https://doi.org/10.3892/etm.2018.6325.

[44] E.E. Mehana, A.F. Khafaga, S.S. El-Blehi, The role of matrix metalloproteinases in osteoarthritis pathogenesis: an updated review, Life Sci. 234 (2019) 116786, https://doi.org/10.1016/j.lfs.2019.116786, 1973.

[45] D.T. Felson, D.R. Gale, M. Elon Gale, J. Niu, D.J. Hunter, J. Goggins, M.P. LaValley, Osteophytes and progression of knee osteoarthritis, Rheumatology 44 (1) (2005) 100–104, https://doi.org/10.1093/rheumatology/keh411.

[46] S. Settle, L. Vickery, O. Nemirovskiy, T. Vidmar, A. Bendele, D. Messing, P. Ruminski, M. Schnute, T. Sunyer, Cartilage degradation biomarkers predict efficacy of a novel, highly selective matrix metalloproteinase 13 inhibitor in a dog model of osteoarthritis: confirmation by multivariate analysis that modulation of type ii collagen and aggrecan degradation peptides parallels pathologic changes, Arthritis Rheumatol. 62 (10) (2010) 3006–3015, https://doi.org/10.1002/art.27596.

[47] A.J. Fosang, K. Last, V. Knäuper, G. Murphy, P.J. Neame, Degradation of cartilage aggrecan by collagenase-3 (MMP-13), FEBS Lett. 380 (1) (1996) 17–20, https://doi.org/10.1016/0014-5793(95)01539-6.

[48] H. Takaishi, T. Kimura, S. Dalal, Y. Okada, J. D'Armiento, Joint diseases and matrix metalloproteinases: a role for MMP-13, Curr. Pharmaceut. Biotechnol. 9 (1) (2008) 47, https://doi.org/10.2174/138920108783497659.

[49] S. Lee, K. Park, S. Lee, J.H. Ryu, J.W. Park, H.J. Ahn, I.C. Kwon, I. Youn, K. Kim, K. Choi, Dark quenched matrix metalloproteinase fluorogenic probe for imaging osteoarthritis developmentin vivo, Bioconjugate Chem. 19 (9) (2008) 1743–1747, https://doi.org/10.1021/bc800264z.